

Wave-packet models for jet dynamics and sound radiation

André V. G. Cavaliere

Associate Professor
Divisão de Engenharia Aeroespacial
Instituto Tecnológico de Aeronáutica
São José dos Campos, SP, Brazil
Email: andre@ita.br

Peter Jordan

Chargé de Recherche
Institut Pprime
Dép. Fluides, Thermique, Combustion
CNRS—Université de Poitiers—ENSMA
Poitiers, France
Email: peter.jordan@univ-poitiers.fr

Lutz Lesshafft

Chargé de Recherche
Laboratoire d'Hydrodynamique (LadHyX)
CNRS—École Polytechnique
Palaiseau, France
Email: lutz@ladhyx.polytechnique.fr

Organised structures in turbulent jets may be modelled as wavepackets. These are characterised by spatial amplification and decay, both of which are related to stability mechanisms, and they are coherent over several jet diameters, thereby constituting a non-compact acoustic source that produces a distinctive directivity in the acoustic field. In this review we use simplified model problems to discuss the salient features of turbulent-jet wavepackets and their modelling frameworks. Two classes of model are considered. The first, that we refer to as kinematic, is based on Lighthill's acoustic analogy, and allows an evaluation of the radiation properties of sound-source functions postulated following observation of jets. The second, referred to as dynamic, is based on the linearised, inhomogeneous Ginzburg-Landau equation, which we use as a surrogate for the linearised, inhomogeneous Navier-Stokes system. Both models are elaborated in the framework of resolvent analysis, which allows the dynamics to be viewed in terms of an input-output system, the input being either sound-source or non-linear forcing term, and the output, correspondingly, either farfield acoustic pressure fluctuations or nearfield flow fluctuations. Emphasis is placed on the extension of resolvent analysis to stochastic systems, which allows for the treatment of wavepacket jitter, a feature known to be relevant for subsonic jet noise. Despite the simplicity of the models, they are found to qualitatively reproduce many of the features of turbulent jets observed in experiment and simulation. Sample scripts are provided and allow calculation of most of the presented results¹

1 Introduction

Jet noise is a fluid-mechanics problem that is both challenging and fascinating on account of the subtlety of the underlying mechanisms. These demand a modelling *finesse* that goes beyond that required in the treatment of most other turbulence problems: whereas in wall-bounded turbulence the main quantity of interest is the time-averaged friction coefficient, which determines the drag of wings and head loss in pipes, turbulent jet noise involves small-amplitude pressure fluctuations far from the nozzle, resolved into frequencies that must be considered over two-to-three decades on account of the high sensitivity of the human ear. A broad range of turbulent scales must therefore be considered, and, specifically, in terms of the manner by which they couple with the acoustic field.

A striking feature of the jet-noise problem is the scale disparity that exists between hydrodynamic and acoustic regions of the flow. Whereas the energetically dominant turbulence structures are relatively small, scaling with the local momentum thickness of the shear layer [1], the acoustic field comprises larger scales, that are, furthermore, more organised. An azimuthal Fourier-series decomposition of the acoustic field in laboratory experiments reveals that low-angle radiation (measured with respect to the downstream jet axis) is predominantly axisymmetric [2, 3, 4, 5], and recent measurements show that this is also the case for full-scale jet engines [6]. Large-eddy simulation data shows that while radiation at higher frequencies does involve higher-order azimuthal modes [7], it nonetheless remains significantly more organised than the turbulence from which it issues. This situation is beautifully illustrated in Figure 1, where the disor-

¹Matlab/Octave scripts are available in ftp://161.24.15.247/Andre/AMR_Wavepackets, and in the Supplementary Material.

ganised turbulence field, highlighted in colour, is observed to drive a more coherent sound field, illustrated in grayscale, and whose shallow-angle component can be seen to be predominantly axisymmetric.

The said scale disparity between the turbulence and sound fields hides an underlying organisation in the turbulent region of the flow. It is the energetic dominance of disparate wavenumbers in each of the fields that leads to the contrast that can be observed both in the simulation snapshot of Figure 1 and in measurements. But careful observation reveals that the hydrodynamic region of the jet comprises an organised structure: there exist coherent, high-amplitude oscillations, saturated in black and white in Figure 1, and that have the form of a wavepacket. This coherent-structure signature has been observed and studied experimentally for over 50 years [9, 10, 11, 12, 13, 14]; a recent observation by Breakey *et al.* [14] is shown in section 3 (Figure 6).

The underlying organisation is more clearly seen when a given azimuthal wavenumber is isolated. Figure 2(a), which shows the axisymmetric component of the pressure field in the same simulation, highlights the wavelike behaviour within the jet. Further simplification results if a single frequency is isolated, and its associated dominant spatial structure deduced; the latter can be obtained as the leading mode of a spectral proper orthogonal decomposition (SPOD), as will be detailed in section 2.4.2. One such leading SPOD mode, for Strouhal number, $St = 0.3$, is shown in Figure 2(b). It takes the form of a wavepacket, with an associated beam of sound energy directed towards low polar angles. The wavepacket was already apparent in the snapshot of the axisymmetric pressure shown in Figure 2(a); but isolating the leading SPOD mode at $St = 0.3$ leads to a cleaner visualisation.

Numerous signal-processing techniques exist for the distillation of flow structures associated with a given frequency-wavenumber pair, and their implementation is facilitated by the availability of multi-probe sensor arrays [15, 16] or field measurements such as particle image velocimetry [1, 17]. The availability of high-fidelity numerical simulation, which allows for the storage of full flow information and quantities that can not be easily measured experimentally, further potentiates these analysis tools [7]. It is of course important to not lose sight of the fact in “isolating” a given frequency-wavenumber component of the flow, complex underlying mechanisms may remain hidden. As discussed in section 2, the non-linearity of the Navier-Stokes system permits interactions between different frequencies and wavenumbers. Fluctuations with low frequencies or azimuthal wavenumbers, with their characteristic wavepacket shape, may therefore comprise dynamics that are coupled to higher frequencies or wavenumbers; in this sense, coherent large-scale structures do not have an autonomous evolution, and are affected, at least to some degree, by incoherent, smaller-scale disturbances. Once this inherent coupling is kept in mind, the decomposition of a turbulent flow into frequencies, wavenumbers and SPOD modes can be seen as a divide-and-conquer strategy, where clearer understanding of the organised structures and their radiated sound is sought,

further work being necessary to study the relationship between these and other structures.

The wave-packet shapes revealed by leading SPOD modes are reminiscent of early flow-visualisation studies of coherent structures in jets [18, 19], where advecting turbulent “puffs” were seen to undergo spatial amplification near the nozzle, followed by downstream decay. This behaviour resembles that of Kelvin-Helmholtz instability in free shear layers, and indeed the first dynamic-modelling attempts involving linear stability analysis [20, 21] were met with some success. But the validity of linear theory applied to turbulent flow, where linearisation is performed by taking the time-averaged mean as base flow, was always a question of debate; Crighton & Gaster [21] argued that “it is natural to attempt an explanation in terms of the instability modes of the mean velocity profile, on the basis that the turbulence establishes an equivalent laminar flow profile as far as large-scale modes are concerned”, but this is clearly a long way from a rigorous demonstration. A twofold approach is therefore necessary, involving a linear stability calculation and an *a posteriori* check of the degree of agreement with reference data. A recent detailed attempt has been carried out by Sasaki *et al.* using high-fidelity simulation data [22].

The possibility of using linear stability theory to model turbulence dynamics is clearly attractive. Due to the interest in laminar-turbulent transition, a substantial body of knowledge exists and has been compiled in monographs [23, 24] and review articles [25, 26, 27]. Linearisation of the flow equations simplifies most of the numerical work, and, perhaps more importantly, leads to a clearer understanding of relevant flow mechanisms, which become analogous to phenomena seen in transition: the growth of structures near the nozzle can, for instance, be associated with the equivalent Kelvin-Helmholtz instability observed in transitional flows. A further interesting possibility is the application of linear control theory [28, 29, 30, 31] to the jet noise problem. However, the said need for an *a posteriori* validity check of linear models remains a drawback.

The recent emergence of *resolvent analysis* in the study of turbulent flows has provided a more solid link between linear models and coherent structures. Following early studies of transitional flows, where the time-domain response of the linearised Navier-Stokes system to stochastic forcing was considered [32, 33], the frequency-domain counterpart, referred to as resolvent analysis, has gained attention recently, initially for wall-bounded turbulence [34, 35] but more recently for turbulent jets [36, 37, 38]. The underlying idea, outlined in section 2.5, involves treatment of the non-linear terms in the flow equations as an external forcing, to which the most linearly amplified flow responses are sought. If the non-linear terms can be approximated as spatially white noise, SPOD modes become identical to the optimal flow responses [36, 37]. This observation suggests a departure point and guide for modelling based on the linearised equations, where focus is on the highest amplification between forcing and response [39]. It also indicates SPOD as the relevant signal-processing method to extract structures for comparison with the results of stability analysis. A detailed com-

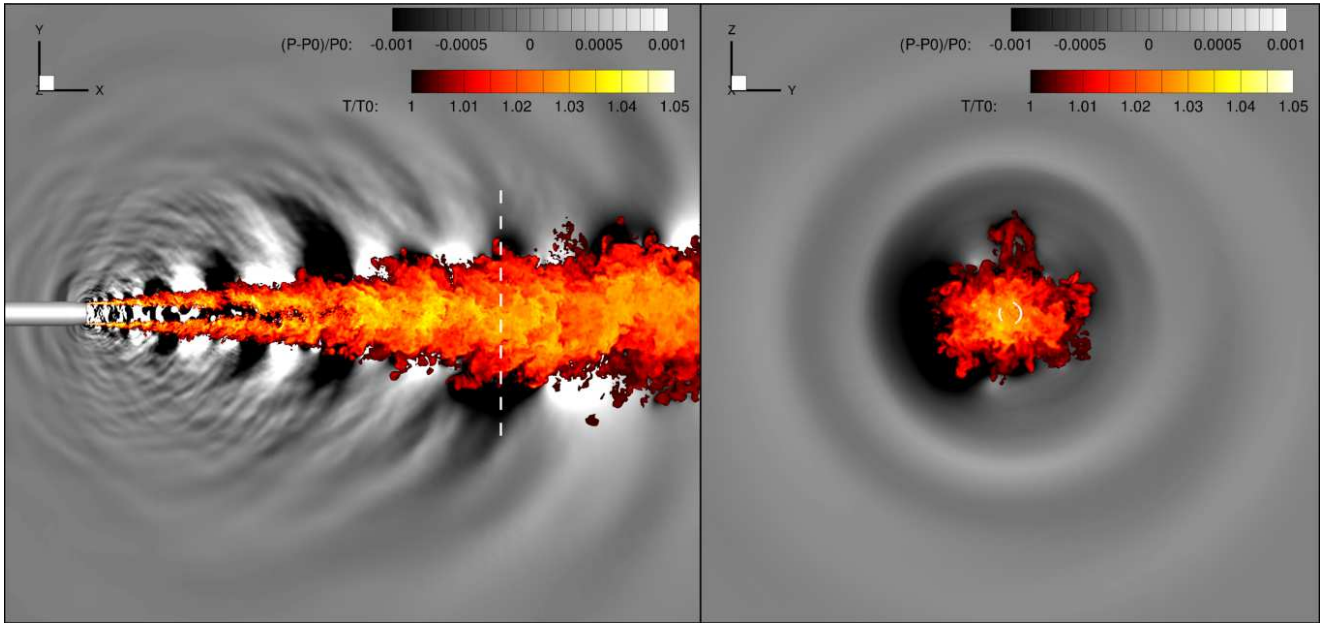


Fig. 1: Illustration of a Mach 0.9 jet and its sound radiation. Colours show temperature fluctuations, highlighting turbulent disturbances, whereas black and white is used for pressure fluctuations, which far from the jet correspond to the acoustic radiation. The right plot shows a cross section of turbulent and acoustic fields taken at $x/D = 20$. Figure taken from the large-eddy simulation of Brès *et al.* [7], using the compressible solver “Charles” [8].

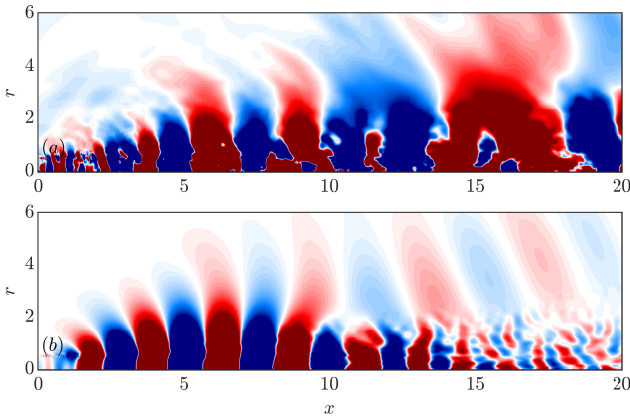


Fig. 2: Wavepackets from the same Mach 0.9 jet simulation shown in figure 1: (a) sample snapshot of the axisymmetric part of the pressure field; (b) pressure from the first SPOD mode at Strouhal 0.3.

parison for turbulent jets has been presented by Schmidt *et al.* [38].

The present review deals with linear modelling frameworks for turbulent-jet wavepacket dynamics and sound radiation. It is a natural follow-on to the recent review article by Jordan & Colonius [40], in so far as we present resolvent analysis (not considered in that review) as a unifying framework, suitable for the consideration of sound radiation by *kinematic* wave-packet sound-source models (where an empirically motivated wavepacket form is postulated and its sound radiation properties evaluated) on one hand, and, on

the other, for the modelling of wavepacket *dynamics*. In the interest of illustrating the key aspects of the modelling frameworks, we restrict our attention to simplified kinematic and dynamic models. The linearised Navier-Stokes system is thus replaced by the linearised Ginzburg-Landau equation. Despite the simplicity of the models, they are found to qualitatively reproduce many of the features of the more complex flows that we are ultimately interested in (and it is this that motivates their consideration). This facilitates a discussion of real flow physics and how these are revealed by the resolvent framework.

The material is organised as follows. In Section 2 we review acoustic and dynamic modelling problems, cast as in terms of forcings and responses that are connected by linear operators, and we discuss the rationale of applying such methods for the study of turbulent flows; we do this in both harmonic and stochastic frameworks. In Section 3 we explore kinematic wave-packet sound-source models, with an emphasis on the key mechanisms underpinning acoustic efficiency. In Section 4 emphasis is on wave-packet dynamics, modelled via stability and resolvent analyses of the linear Ginzburg-Landau equation. Finally, in Section 5 we couple the analyses of Sections 3 and 4, showing how the non-linear forcing terms can be connected to the radiated acoustic field.

As mentioned above, we have chosen to work with simplified models, in the spirit of numerous previous studies concerned with transition and turbulence [41, 42, 43], and supplementary material is provided in the form of scripts for Matlab/Octave that allow the main results of the paper to be reproduced, facilitating a thorough understanding of the underlying concepts and models. Our goal is twofold. On one hand, the simplicity of the models is such that the ma-

terial may serve as a useful starting point for readers new to the field; extension of the methods to real jets is a tedious but straightforward task. On the other, the capacity of the simple models to provide (a sometimes remarkable) qualitative reproduction of what is observed in Navier-Stokes flow physics, suggests that they, or suitably enhanced variants, be seriously considered as a means by which to probe the mysteries of the jet-noise problem.

2 Fundamentals of linear models applied to the jet-noise problem

2.1 Lighthill's acoustic analogy

Lighthill's acoustic analogy [44] is based on a rewriting of the continuity and Navier-Stokes system for a compressible flow such that they take the form of an inhomogeneous wave equation,

$$\frac{\partial^2 \rho}{\partial t^2} - c_0^2 \Delta \rho = \frac{\partial^2 T_{ij}}{\partial x_i \partial x_j}, \quad (1)$$

where $T_{ij} = \rho u_i u_j + \delta_{ij}(p - c_0^2 \rho) + \tau_{ij}$ is Lighthill's stress tensor, ρ is the fluid density, u_i are the velocity components in a Cartesian system, t is time, x_i are Cartesian coordinates, c_0 is the speed of sound and τ_{ij} are viscous stresses; Einstein's summation is implied. In operator notation, this can be written as,

$$\mathcal{L}_{\text{wave}}[\rho(\mathbf{x}, t)] = S(\mathbf{x}, t). \quad (2)$$

The basic idea behind the approach is to split the compressible Navier-Stokes system into the linear wave (or d'Alembert) operator $\mathcal{L}_{\text{wave}}$, with well-known properties, forced by the right-hand-side source terms S which are more complex, involving products of flow fluctuations. The solution of the system can be obtained by appealing to the Green's function, or impulse response, solution of,

$$\mathcal{L}_{\text{wave}}[G(\mathbf{x}, t, \mathbf{y}, \tau)] = \delta(\mathbf{x} - \mathbf{y}, t - \tau), \quad (3)$$

which can then be used to solve equation 1 for an arbitrary source distribution, $S(\mathbf{x}, t)$, in the absence of solid boundaries, via,

$$\rho(\mathbf{x}, t) = \int S(\mathbf{y}, \tau) G(\mathbf{x}, t, \mathbf{y}, \tau) d\mathbf{x} d\tau, \quad (4)$$

with an integral over space and time.

Instead of working in the time domain, it is often useful to write Lighthill's analogy in the frequency domain. It is straightforward to apply a Fourier transform in time, as the operator is stable (i.e. an arbitrary initial condition does not lead to exponential fluctuation growth) and has constant

coefficients in time; in this case, time is said to be a homogeneous direction. Defining direct and inverse Fourier transform of a function $f(t)$, respectively, by,

$$\hat{f}(\omega) = \int_{-\infty}^{\infty} f(t) e^{i\omega t} dt, \quad (5)$$

and,

$$f(t) = \frac{1}{2\pi} \int_{-\infty}^{\infty} \hat{f}(\omega) e^{-i\omega t} d\omega, \quad (6)$$

Fourier transform of eq. (2) leads to an inhomogeneous Helmholtz equation, which can be written for pressure fluctuations as,

$$\mathcal{L}_{\text{Helmholtz}}[\hat{p}(\mathbf{x}, \omega)] = \hat{S}(\mathbf{x}, \omega), \quad (7)$$

with solution given by,

$$\hat{p}(\mathbf{x}, \omega) = \int S(\mathbf{y}, \omega) G(\mathbf{x}, \mathbf{y}, \omega) d\mathbf{x}, \quad (8)$$

where here the Green's function is the impulse response of the Helmholtz equation. Properties of this equation have been thoroughly reviewed by Crighton [45], who provides expressions for the Green's functions of the wave and Helmholtz equations in one, two and three dimensions.

Solutions obtained using the Green's function, such as eqs. (4) and (8), can be thought of as inversions of the linear differential operator \mathcal{L} , which becomes an integral operator upon inversion. This operator is referred to as the *resolvent*. For instance, eq. (8) can be written in operator notation, as,

$$p = \mathcal{R}_{\text{Helmholtz}}[S], \quad (9)$$

where we have dropped hats and dependent variables in the interest of keeping the notation compact. The resolvent operator, given by,

$$\mathcal{R}[\cdot] = \int [\cdot] G(\mathbf{x}, \mathbf{y}, \omega) d\mathbf{x}, \quad (10)$$

allows the problem to be cast in an input-output framework. For a spatial integration approximated using quadrature weights, W , the resolvent can be approximated as,

$$\mathbf{R} = \mathbf{G}\mathbf{W}. \quad (11)$$

With the integral operators above, the effect of a postulated source distribution S (the input) on the radiated pressure p (the output) can be studied. Lighthill [44] followed such an approach by postulating inputs describing compact sources

— eddies with characteristic length much smaller than the acoustic wavelength. By doing so he obtained approximate trends for the velocity dependence of the radiated sound.

A more systematic approach for the study of input-output relationships such as the above has become popular recently. It is based on finding an input, with unit norm, that maximises the output [25]. For Lighthill’s analogy this amounts to finding a source distribution that would maximise the radiated sound. This will be further explored in section 2.3.

2.2 Resolvent analysis

Lighthill’s idea can be elaborated in a more general context, where one uses the linearised Navier-Stokes operator instead of the d’Alembertian. This can be used to study sound generation and refraction in a shear flow [46] or to explore the dynamics of turbulence in a simpler context, aided by a linear operator [32, 34, 47]. In what follows we consider the latter approach in the framework of incompressible flow².

The Navier-Stokes system,

$$\frac{\partial u_i}{\partial t} + u_j \frac{\partial u_i}{\partial x_j} = -\frac{\partial p}{\partial x_i} + \frac{1}{Re} \nabla^2 u_i, \quad (12)$$

supplemented by the incompressibility constraint, $\partial u_i / \partial x_i = 0$, can be Fourier transformed³, leading to,

$$-i\omega \hat{u}_i + U_j \frac{\partial \hat{u}_i}{\partial x_j} + \hat{u}_j \frac{\partial U_i}{\partial x_j} + \frac{\partial \hat{p}}{\partial x_i} - \frac{1}{Re} \nabla^2 \hat{u}_i = - \left[\hat{u}_j * \frac{\partial \hat{u}_i}{\partial x_j} \right]_{\omega \neq 0}. \quad (13)$$

The Fourier transform of the non-linear convective term in the time-domain equation (12) leads to a convolution (denoted by $*$), which in eq. (13) is split into two parts. Terms involving the $\omega = 0$ component, which is the mean flow, U , are written on the left-hand side, and the remaining part of the convolution is retained on the right-hand side inside square brackets. The full convolution can be written as,

$$\left[\hat{u}_j * \frac{\partial \hat{u}_i}{\partial x_j}(\omega) \right] = \int_{-\infty}^{\infty} \hat{u}_j(\omega - \omega_0) \frac{\partial \hat{u}_i}{\partial x_j}(\omega_0) d\omega, \quad (14)$$

where we recognise that the integral involves products of quantities taken at frequencies, $\omega_a = (\omega - \omega_0)$ and $\omega_b = \omega_0$ whose sum is the “target” frequency ω (the usual triads in non-linear interactions). We thus see that a given frequency component depends on others due to the non-linear term.

²This choice is motivated by the more compact system for incompressible flow; however, a similar approach can be taken for compressible jets [48, 49, 50, 38, 51].

³Besides taking a Fourier transform from time to frequency, whenever a spatial direction is periodic and homogeneous it is appropriate to take a further Fourier series. The usual example is the azimuth for jets and pipes, which can be transformed into azimuthal modes as a function of circumferential wavenumber m . The present analysis can be extended to other directions in a straightforward manner, keeping in mind that convolutions should then be taken in all Fourier-transformed variables.

The underlying idea is the same as Lighthill’s: the left-hand side is the simpler linearised Navier-Stokes operator, and the right-hand side involves products of flow fluctuations. In operator notation, this can be written as,

$$\mathcal{L}_{\text{N-S}}[\mathbf{q}] = \mathbf{f}, \quad (15)$$

where \mathbf{q} is a vector comprising velocity and pressure, and the right-hand side, with all its complexity, has been lumped into a forcing term, \mathbf{f} . The solution can be written schematically as,

$$\mathbf{q} = \mathcal{R}_{\text{N-S}}[\mathbf{f}], \quad (16)$$

where $\mathcal{R}_{\text{N-S}}$ is the resolvent operator, synonymous with the Green’s function of the linearised Navier-Stokes system. The solution of the frequency-domain problem is straightforward if the base flow, U , is globally stable: a periodic forcing, $\mathbf{f}(\omega)$, leads to a periodic response, $\mathbf{q}(\omega)$. Of course one cannot claim that the Navier-Stokes system has been solved as such, as the convolution has been replaced by a somewhat artificial forcing term. However, writing the problem in this form is useful, as it allows study of the input-output relationship between the non-linear terms and associated flow responses.

If the base-flow about which linearisation is performed is homogeneous in one or more spatial directions, the linearised operator, \mathcal{L} , has constant coefficients in these directions, which can be Fourier transformed. Eq. 16 then relates a frequency-wavenumber pair in the forcing to the same pair in the response. The Helmholtz equation is homogeneous in all spatial directions, and thus a complete analysis can be performed in frequency-wavenumber space; eq. (16) becomes a scalar equation whose solution is straightforward. Fourier modes thus become the natural basis in which to express inputs and outputs. This approach is reviewed in detail by Crighton [45].

Finding an analytical Green’s function for the linearised Navier-Stokes operator is not straightforward. Frequency domain Green’s functions can be derived for parallel base flows via the signalling problem, outlined by [52], and which can be extended to slowly-diverging flows using the WKB method [53, 54]. However, for a more general base flow, finding the resolvent operator numerically seems the more suitable approach. Eq. (15) can be discretised as $\mathbf{L}\mathbf{q} = \mathbf{f}$, where \mathbf{L} is the matrix representation of the discretised operator, including the boundary conditions of the problem. The discretised resolvent operator is then simply, $\mathbf{R} = \mathbf{L}^{-1}$.

An important point to note is that restrictions can be imposed on the forcing terms, as certain quantities, or regions of space, in the output may be of more interest than others. To see how this fits the resolvent framework above, it is useful to recast eq. (16) in state-space form, similar to what is

done in control theory,

$$\begin{aligned}\frac{\partial \mathbf{q}}{\partial t} &= \mathbf{A}\mathbf{q} + \mathbf{B}\mathbf{f}, \\ \mathbf{y} &= \mathbf{C}\mathbf{q},\end{aligned}\quad (17)$$

where \mathbf{A} is the linearised Navier-Stokes operator (without the time derivatives of state variables), the operator \mathbf{B} imposes restrictions or weights on possible forcings, and the operator \mathbf{C} selects a relevant output, \mathbf{y} . For instance, \mathbf{B} can restrict the forcing to be zero in regions where non-linear terms are expected to vanish, and \mathbf{C} can select a flow quantity and/or a region of interest, such as the pressure in the acoustic field, which can be obtained as a relevant output if \mathbf{A} is the compressible Navier-Stokes operator.

Writing eq. (17) in the frequency domain, considering that \mathbf{A} is stable, leads to a transfer function between \mathbf{y} and \mathbf{f} ,

$$\mathbf{y}(\omega) = \left[\mathbf{C}(-i\omega\mathbf{I} - \mathbf{A})^{-1}\mathbf{B} \right] \mathbf{f}(\omega), \quad (18)$$

and the resolvent, including \mathbf{B} and \mathbf{C} operators, can be written as $\tilde{\mathbf{R}} = \mathbf{C}\mathbf{R}\mathbf{B}$, where $\mathbf{R} = (-i\omega\mathbf{I} - \mathbf{A})^{-1}$ is the full-forcing/full-state resolvent (with $\mathbf{B} = \mathbf{C} = \mathbf{I}$). In what follows we will most often refer to \mathbf{R} , but inclusion of arbitrary restrictions to inputs and outputs is straightforward, the resolvent operator being simply replaced by $\tilde{\mathbf{R}}$.

2.3 Harmonic forcing and singular-value decomposition

We now consider problems cast in the form of eqs. (9) or (16), the former relating sound radiation to turbulent fluctuations, the latter relating turbulent fluctuations to non-linear forcing terms. In particular, we evaluate the flow response to a given time-periodic forcing; we study thus the harmonic response of the flow, similar to early experiments where jet turbulence was studied by imposing an external periodic excitation [18, 19, 55].

When discretised, the resolvent operator becomes a matrix, and the input-output formulation can be written as,

$$\mathbf{q} = \mathbf{R}\mathbf{f}. \quad (19)$$

To systematically obtain a relationship between inputs and outputs, it is useful to consider the singular-value decomposition (SVD) of \mathbf{R} , given by,

$$\mathbf{R} = \mathbf{U}\mathbf{S}\mathbf{V}^H, \quad (20)$$

where the superscript H indicates the Hermitian transpose of a matrix. SVD decomposes \mathbf{R} into two unitary matrices, \mathbf{U} and \mathbf{V} , i.e.,

$$\mathbf{U}^H\mathbf{U} = \mathbf{V}^H\mathbf{V} = \mathbf{I}, \quad (21)$$

meaning that each matrix has columns forming an orthonormal basis in terms of the standard Euclidean inner product, $\langle \mathbf{f}, \mathbf{g} \rangle = \mathbf{g}^H\mathbf{f}$. For reasons that will soon become apparent, we refer to \mathbf{U} and \mathbf{V} as output and input bases, respectively. The matrix \mathbf{S} is diagonal, with real, positive values,

$$\mathbf{S} = \begin{bmatrix} \sigma_1 & 0 & \cdots & 0 \\ 0 & \sigma_2 & \cdots & 0 \\ \vdots & \vdots & \ddots & \vdots \\ 0 & 0 & \cdots & \sigma_n \end{bmatrix}, \quad (22)$$

such that $\sigma_1 \geq \sigma_2 \geq \sigma_3 \geq \cdots \geq \sigma_n$.

From the above, we obtain,

$$\mathbf{q} = \mathbf{U}\mathbf{S}\mathbf{V}^H\mathbf{f} \implies \mathbf{U}^H\mathbf{q} = \mathbf{S}\mathbf{V}^H\mathbf{f}, \quad (23)$$

which indicates that the projection of the response, \mathbf{q} , onto each vector of basis U is equal to the projection of the forcing, \mathbf{f} , onto each vector of basis V times the corresponding gain, σ . For instance, if the forcing is given by $\mathbf{f} = v_1$, where v_1 is the first vector of basis V , the flow response is, $\mathbf{q} = \sigma_1 u_1$, i.e. σ_1 times the first vector of basis U . The pair v_1, u_1 thus comprise the optimal forcing and the most amplified response, respectively. The gain, σ_1 , is the ratio between the norms of response and forcing in this case, and is therefore the maximum amplification for a given input, \mathbf{f} . It is thus possible to characterise the harmonic input-output problem by building a hierarchy of orthogonal forcing functions, ordered from the optimal (v_1) to the suboptimal forcings (v_2, v_3, \dots), and a corresponding hierarchy of orthogonal flow responses. Bearing in mind that this comes from an analysis of the problem with time-periodic forcing, it becomes clear that the response of a flow to an arbitrary harmonic excitation is dominated by the optimal response u_1 if $\sigma_1 \gg \sigma_n, n \geq 2$.

2.4 Response to stochastic forcing

2.4.1 Frequency-domain statistics

The above analysis is meaningful for evaluation of flow responses when some external forcing, periodic in time, is imposed. In a general turbulent flow, fluctuations are stationary random functions, which can be meaningfully characterised either via single-point statistics such as the mean, the variance or the autocorrelation function; or in terms of two-point statistics, via the cross-correlation function. In the frequency domain, the most complete description of two-point statistics is provided by the cross-spectral density function,

⁴In the continuous case, one often has an inner product of functions given by, $\langle \mathbf{f}, \mathbf{g} \rangle = \int g^*(\mathbf{x})f(\mathbf{x})d\mathbf{x}$. The discretised form of the integral leads to, $\langle \mathbf{f}, \mathbf{g} \rangle = \mathbf{g}^H\mathbf{W}\mathbf{f}$, where \mathbf{W} is a diagonal matrix of quadrature weights that approximates the integral in the inner product. Resolvent analysis and proper orthogonal decomposition are modified to account for the quadrature weights. Appropriate equations can be found in [50, 37], for instance. In what follows we will neglect such quadrature weights to simplify notation; however, the sample scripts used in the examples of this paper make use of the weight matrix.

which is the Fourier transform of the cross-correlation function [56], but can also be defined as the expected value,

$$P_{qq} = \mathcal{E}(qq^H), \quad (24)$$

where q here denotes a Fourier transform taken for a given realisation, and \mathcal{E} is the expected-value operator, which amounts to an average of several realisations. Once q is discretised, P_{qq} becomes a cross-spectral-density matrix, which is Hermitian; its main diagonal contains the real, positive power spectral densities (PSDs) of flow quantities at given spatial locations. Moreover, the cross-spectral density, P_{qq} , for a given quantity at points y_1 and z_1 , can be decomposed as,

$$P_{qq}(y_1, z_1) = \sqrt{P_{qq}(y_1, y_1)} \sqrt{P_{qq}(z_1, z_1)} e^{i\phi_{12}} \gamma(y_1, z_1), \quad (25)$$

i.e. the product of square roots of PSDs at positions y_1 and z_1 , an exponential of the averaged phase difference, ϕ_{12} , and the coherence function, γ , defined as,

$$\gamma^2(y_1, z_1) = \frac{|P_{qq}(y_1, z_1)|^2}{P_{qq}(y_1, y_1)P_{qq}(z_1, z_1)}. \quad (26)$$

We see that the coherence function is a normalised absolute value of the CSD, taking values between 0 and 1. Perfectly periodic oscillations have unit coherence, and thus γ is a metric for the loss of synchronicity between a pair of positions. In a turbulent flow, when y_1 and z_1 are sufficiently far from one another the coherence decays to zero, and one has perfectly incoherent oscillations at the two distant points. Such a description is appropriate when flow statistics are considered in the frequency domain. Given the use of expected values, one should think of amplitudes and phases as quantities that are averaged over realisations, and the amount of variance, or randomness, between realisations is measured by the coherence function.

Finally, for later use, we can define *white noise in space* for a given frequency, ω , as the CSD given by,

$$P_{qq}(y_1, z_1) = \begin{cases} 1 & \text{if } y_1 = z_1, \\ 0 & \text{otherwise.} \end{cases} \quad (27)$$

Such a CSD implies a constant PSD, equal to 1, everywhere, and perfectly incoherent fluctuations for any non-coincident positions. This CSD, once discretised, becomes the identity matrix I .

2.4.2 Spectral proper orthogonal decomposition (SPOD)

The cross-spectral density can be decomposed in a useful manner by taking its eigenvalue decomposition, which is referred to as spectral proper orthogonal decomposition

(SPOD). Its time-domain variant is termed simply POD, and has been extensively applied in fluid mechanics; see for instance Berkooz *et al.* [57], or the recent reviews by Rowley & Dawson [58], Taira *et al.* [59]. For our purposes, the frequency-domain counterpart, SPOD, is preferred, as discussed above, due to its relationship to resolvent analysis, which will be explored later. It can be obtained by solving the integral eigenvalue problem [60],

$$\int_{\mathcal{V}'} P_{qq}(\mathbf{x}, \mathbf{x}', \omega) \mathbf{q}_{SPOD}(\mathbf{x}', \omega) d\mathbf{x}' = \lambda \mathbf{q}_{SPOD}(\mathbf{x}, \omega), \quad (28)$$

where integration is performed over a region of space, \mathcal{V}' , a volume in the most general case. The eigenfunction, $\mathbf{q}_{SPOD}(\mathbf{x}, \omega)$, is an SPOD mode and λ its eigenvalue. The discretised form of the above equation is,

$$P_{qq} W \mathbf{q}_{SPOD} = \lambda \mathbf{q}_{SPOD}. \quad (29)$$

In the simpler case of uniform integration weights, $W = \Delta x I$ can be absorbed as a constant multiplying the cross-spectral matrix P_{qq} ⁵, and the problem is then simply written as the diagonalisation of the Hermitian CSD,

$$P_{qq} = Q_{SPOD} \Lambda Q_{SPOD}^H, \quad (30)$$

where Q_{SPOD} is a unitary matrix — an orthonormal basis of SPOD modes contained in the columns of the matrix, such that $Q_{SPOD}^H Q_{SPOD} = I$ — and Λ is a diagonal matrix of real, positive eigenvalues, λ_i , such that $\lambda_1 \geq \lambda_2 \geq \lambda_3 \geq \dots$. The SPOD modes provide an orthonormal basis that is optimal for representation of the overall power spectra: the first mode represents an integrated PSD equal to λ_1 , and so on [57, 60, 37].

2.4.3 Stochastic forcing and resolvent analysis

The response of a flow to stochastic forcing, $P_{ff} = \mathcal{E}(ff^H)$, can also be obtained using the resolvent operator, via,

$$P_{qq} = \mathcal{E}(qq^H) = \mathcal{E}(R f f^H R^H) = R P_{ff} R^H, \quad (31)$$

which relates the CSD of the flow response, P_{qq} , to the CSD of the forcing, P_{ff} . Singular-value decomposition of the re-

⁵Even for non-uniform weights, eq. (29) leads to orthogonal eigenfunctions and real, positive eigenvalues. To see this, eq. (29) can be rewritten, by pre-multiplication by the Cholesky decomposed weights $W^{1/2}$, as $W^{1/2} P_{qq} W^{1/2} W^{1/2} Q_{SPOD} = W^{1/2} Q_{SPOD} \Lambda$; considering $\tilde{P}_{qq} = W^{1/2} P_{qq} W^{1/2}$ (a Hermitian matrix) and $\tilde{Q}_{SPOD} = W^{1/2} Q_{SPOD}$, we have the modified eigenvalue problem $\tilde{P}_{qq} \tilde{Q}_{SPOD} = \tilde{Q}_{SPOD} \Lambda$, which is the eigenvalue decomposition of the Hermitian matrix \tilde{Q}_{SPOD} . Once the problem is solved numerically, the SPOD modes are recovered as $Q_{SPOD} = W^{-1/2} \tilde{Q}_{SPOD}$, and satisfy orthonormality with respect to the weighted inner product, $Q_{SPOD}^H W Q_{SPOD} = I$. Non-uniform weights appear for a non-uniform grid, or, for jet problems, due to the appearance of the radius inside the volume integral, as discussed by Jung *et al.* [15].

solvent operator gives,

$$P_{qq} = USV^H P_{ff} V S U^H, \quad (32)$$

where we note that the CSD of the flow response can be written as a function of the response modes from resolvent analysis, once a given forcing CSD has been projected onto the forcing modes via the term $V^H P_{ff} V$.

An interesting simplification is obtained by considering spatially white forcing, such that $P_{ff} = I$. One then obtains,

$$P_{qq} = US^2 U^H, \quad (33)$$

which, on comparison with eq. (30), reveals an identity between the SPOD modes and the response modes from resolvent analysis, with SPOD eigenvalues equal to the square of the resolvent gains [36, 37].

A last remark can be made regarding systems in which the optimal forcing-response pair dominates, i.e. when σ_1 is much larger than the suboptimal resolvent gains. In that case, an arbitrary forcing CSD, P_{ff} , with non-zero projection onto the optimal forcing, v_1 , leads to a response CSD, P_{qq} , dominated by the most amplified response, u_1 . A highly amplified flow response is thus likely to appear in the flow statistics regardless of specific forcing statistics.

2.5 Overview of input-output analysis

In the foregoing we have developed the basic tools required for a simplified analysis of turbulent-jet dynamics and sound radiation. Inputs (source terms in an acoustic analogy, non-linear interaction terms in the Navier-Stokes system, both treated as external forcings) lead to a flow response (sound radiation, flow fluctuations) via the resolvent operator. The properties of the resolvent operator thus determine the selection of relevant inputs for a given problem, those that lead to significantly amplified responses.

One should bear in mind that the input terms are themselves non-linear functions of the output variables. This is shown schematically in figure 3 for the linearised Navier-Stokes system. Inputs are constructed by applying the non-linear operator \mathcal{N} , for given frequency, ω , and azimuthal wavenumber, m , to the flow fluctuations, \mathbf{q}' . This leads to flow responses $\tilde{\mathbf{q}}$ through the resolvent operator $\mathcal{R} = \mathcal{L}^{-1}$. Such flow responses combine in the non-linear convective term, which thus recycles responses as forcing terms. The resolvent operator is based on a linearisation around the mean flow, $\bar{\mathbf{q}}$, which can be obtained with the Reynolds-averaged ($\omega = 0, m = 0$) Navier-Stokes, or RANS, equations. Alternatively, the mean flow can be separately obtained from an experiment or high-fidelity simulation.

Solution of the system requires a simultaneous solution for all frequencies and wavenumbers, in a procedure that would not be simpler than direct numerical or large-eddy simulation. However, the analysis of a single row of the system — i.e. a given frequency-wavenumber pair — provides relevant information, especially if the resolvent operator has a gain separation, with $\sigma_1 \gg \sigma_{2,3,\dots}$. Such a gain

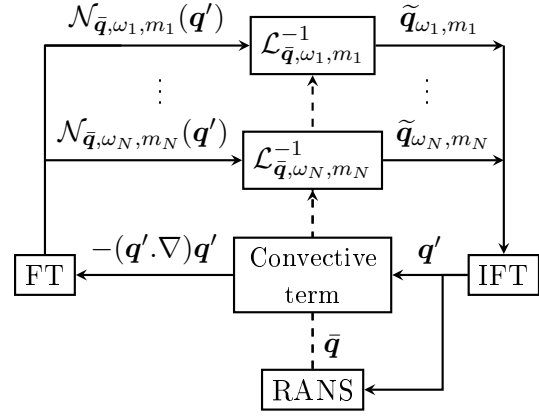


Fig. 3: Schematic representation of resolvent analysis for a turbulent jet. FT and IFT stand for the Fourier transform and its inverse, respectively. Figure taken from Tisot *et al.* [50]

separation may occur when the system is forced with a given (ω, m) pair close to an eigenvalue of the linearised operator, for which $\mathcal{L}(q) = 0$ has a non-trivial solution $q \neq 0$: if (ω, m) are close to such an eigenvalue, \mathcal{L} is close to singular, leading to high gains corresponding to the usual phenomenon of resonance. This is more clearly observed in the system written in state-space form (17), where the transfer function in eq. (18) approaches infinity if the frequency ω is close to an eigenvalue ω_0 of the system, such that $\mathbf{A}\mathbf{q}_0 = -i\omega_0\mathbf{q}_0$ for some non-zero eigenfunction \mathbf{q}_0 ; in this case, the linear operator $\mathbf{L} = (-i\omega\mathbf{I} - \mathbf{A})$ becomes singular at $\omega \rightarrow \omega_0$ (i.e. it has a zero singular value, associated with the eigenfunction, q_0) and the leading gain of $\mathbf{R} = (-i\omega\mathbf{I} - \mathbf{A})^{-1}$, which is the inverse of the smallest singular value of \mathbf{L} , goes to infinity.

If the linearised operator is non-normal, or not self-adjoint, eigenfunctions are not orthogonal and significant gains may be obtained even far from resonance. Detailed discussion of non-normality can be found in [32, 61, 25, 29, 27]. The linearised Navier-Stokes operator with a sheared base flow has a marked non-normal behaviour at high Reynolds numbers. This leads to the aforementioned high gains between forcing and response, with the optimal forcing leading to an amplification significantly higher than that produced by the suboptimals. As a consequence, a general stochastic forcing tends to lead to a flow CSD dominated by the leading response mode, as discussed in section 2.4.3, and in this case a turbulent flow would have a clear presence of coherent structures, which can be thought of as the most likely response to stochastic forcing that would arise in a turbulent field, on account of its high relative gain, or amplification. For jets, the most prominent structures are Kelvin-Helmholtz wavepackets, which have been observed since early flow visualisation experiments [18, 19], and today can be characterised in detail thanks to more advanced experimental diagnostics [16, 1, 17] or simulations [22, 38]; as we discuss in section 4, such wavepacket structures can be obtained accurately as the leading response mode of the resolvent operator. For modelling purposes, to obtain such a dominant response the specific details of the forcing statistics, P_{ff} , are not so rel-

evant, as discussed by Farrell & Ioannou [32,62] and Benedine *et al.* [63]. However, if a detailed characterisation of the response CSD is necessary, then an accurate model of P_{ff} is also likely to be necessary.

As discussed in the Introduction and in section 2.2, non-linear interactions are implicit in the forcing term, which involves a convolution. For given (ω_0, m_0) , the forcing term will be formed by all pairs of frequencies (ω_a and ω_b , say) and wavenumbers (m_a and m_b) whose sums satisfy $\omega_a + \omega_b = \omega_0$ and $m_a + m_b = m_0$, referred to as triads. Resolvent analysis, as we describe it here, does not elucidate the relevant non-linear interactions associated with the dynamics of turbulent structures, since it lumps all interactions into a single forcing term. Some work on jet noise, such as Wu & Huerre [64] and Sponitsky *et al.* [65,66] have looked more directly into the role of nonlinearity in jet dynamics and sound radiation, by taking one or more triads and exploring how wavenumber-frequency pairs can lead to sound radiation. This is a promising but challenging approach, as it is crucial to restrict the ensemble of nonlinear interactions to some manageable size; otherwise, the complexity and computational cost may rise to those of a large-eddy simulation. Another possibility is to probe the non-linear terms of a full simulation, to evaluate how the forcing term in the resolvent analysis is built from the bulk of interactions in the turbulence. Some analysis of this kind has been performed by Towne *et al.* [67].

In what follows we use the input-output characteristics of acoustic (eq. 7) and hydrodynamic (eq. 15) systems to explore the responses that arise due to particular forcings. For the acoustic problem, the simplicity of the linearised operator, whose Green's function is available analytically, allows an analysis of the sound radiation by a wavepacket source, chosen to mimic the Kelvin-Helmholtz structures that are observed in turbulent jets. The hydrodynamic problem is comparatively more complex, but the non-normality of the linearised operator simplifies the analysis, due to the dominance of the leading forcing-response pair. These methods will be elaborated using simplified model problems, that qualitatively represent the essential features of jet dynamics and sound radiation, as discussed in the Introduction. We start by studying the acoustic problem in section 3, followed by analysis of the hydrodynamic system with a model problem in section 4.

3 Kinematic wavepacket models

As discussed in the Introduction, the first observations of coherent structures in turbulent jets [68, 10, 18] were accompanied by the proposition that these might be important for sound generation [69, 9, 11, 12], on one hand, and dynamically underpinned by the stability properties of the mean flow [21], on the other. The former idea can be explored using acoustic-analogy-based (kinematic) wavepacket sound-source models [9, 70, 71, 45, 72, 5, 73, 74]. These are frequently considered in the form of a line distribution, the justification of which will be discussed. Using the line-source model as a workhorse, we will focus on two aspects: (1) the

wavepacket features that underpin acoustic efficiency; and, (2) the extent to which this simple model has been useful in explaining/interpreting experimental observations.

Discussion of the first point requires that we consider the notion of acoustic matching, first evoked by Ffowcs-Williams [75], later by Crighton [45], and which has been used to perform numerous analyses of numerical [76,77] and experimental [17] data, or to interpret behaviour observed in model problems [74, 78, 79]. Acoustic matching is a particular case of the more general filtering operation that underpins the action of the resolvent operator, discussed in section 2. The central idea, details of which will be given later, can be summarised as follows. The solution of the inhomogeneous wave equation, Eq. 4, connects the source field, $\hat{S}(\mathbf{y}, \tau)$, to the sound field, $\hat{p}(\mathbf{x}, t)$, via a convolution. It is useful to see the convolution as a filtering of the source by the Green's function. The filtering extracts from the source field those space and time scales that match (or drive) those supported by the wave equation (propagating sound waves). In the more general case of the inhomogeneous, linearised Navier-Stokes system, the resolvent operator similarly filters the non-zero-frequency, non-linear dynamics that match (or drive) linear dynamics supported by the linearised Navier-Stokes equations.

In what follows we elaborate the line-source wavepacket modelling framework, from its single-point, time-periodic form to its two-point, stochastic form, using simple examples to illustrate the key ideas. On account of an intriguing and important difference between subsonic and supersonic jets, and with a view to elucidating the underlying mechanisms and consequences for dynamic modelling, we systematically compare wavepackets in jets of Mach number, $M = 0.6$ and $M = 2$; the associated convective Mach number M_c , given by the ratio of the phase speed of the wavepacket and the ambient speed of sound, is approximated here as $0.6M$. This gives, for the subsonic and supersonic cases, respectively, $M_c = 0.36$ and $M_c = 1.2$.

3.1 The line-source model

The complete sound-source term of equation 1 is a nine-component tensor involving the double divergence of velocity products. The difficulty of clarifying its link with the sound field is nicely resumed by Mollo-Christensen: "*An experimenter looking at Eq. (3) [cf. Fig 4] is not going to be very happy. It tells him that the pressure time correlation in the far field, which he can measure using a single microphone and some electronic gadgetry, can also be found by measuring quadruple space-time correlations of the velocity fluctuations for all pairs of points \vec{x} and \vec{y} within the jet, and then evaluating the sextuple integral [9].*"

Simplification is necessary, and, in the spirit of another of Mollo-Christensen's comments, perhaps even a *quasi-moral obligation*: "*If you think you know some of the features of a random function, for goodness sake put them in.*" [9]. With that in mind, the following observations are of interest:

1. As mentioned in the foregoing discussion of figure 1, the sound field of a turbulent jet is dominated by only three

$$\begin{aligned}
\langle p(\vec{r}, t) p(\vec{r}, t + \tau) \rangle &= R_{pp}(\vec{r}, t) \\
&= \frac{2 \nu_a \nu_s \nu_r \nu_s}{(4\pi)^2 |\vec{r}|^6} \iiint_{V_x} \iiint_{V_y} \frac{\partial^4}{\partial z^4} \langle T_{ij}(\vec{x}, t_x) T_{\omega_3}(\vec{y}, t_y + \tau) \rangle dV_x dV_y \quad (3)
\end{aligned}$$

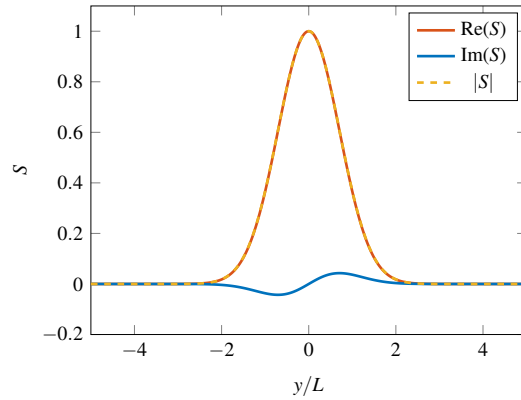
Fig. 4: Mollo-Christensen's handwritten solution of equation 1 for the farfield sound-pressure auto-correlation [9].

azimuthal Fourier modes, $m = 0, \pm 1$ & ± 2 , suggesting that the same three azimuthal modes of the sound source dominate the generation of sound [3, 80, 5].

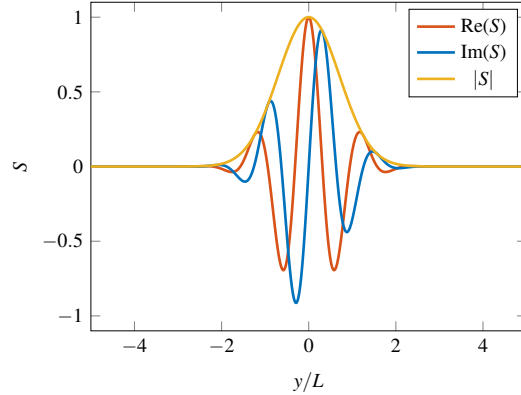
2. A theoretical analysis by Michalke & Fuchs [11] indicates why this is: higher-order azimuthal modes are acoustically inefficient because of destructive azimuthal interference.
3. Coherent structures in turbulent jets, illustrated in figure 2, are observed to comprise convected, wave-like disturbances whose amplitudes grow and then decay over space scales considerably larger than the integral turbulence scales, but comparable with the wavelength of sound at similar frequencies; this makes the jet acoustically non-compact in the streamwise direction [68, 60, 16, 13, 81, 82, 1, 14].
4. In the radial direction, on the other hand, the jet is acoustically compact for the most energetic, low-frequency, sound radiation [5].
5. For low-frequency radiation to low polar angles the axisymmetric mode of the $ij = 11$ component of the linearised Lighthill stress tensor dominates [83].

These are the pivotal arguments that motivate use of the simplified model functions we explore in what follows, which are intended to qualitatively replicate the dominant sound-producing source features. Noting that the highest levels of sound are radiated at low-frequency to low polar angles, points 4 & 5 justify that the model function be restricted to a line, while point 3 suggests a form for its streamwise dependence. Point 5, furthermore, suggests that the model be restricted to the streamwise component of the linearised source term, which is proportional to the streamwise velocity fluctuation. The jet as a sound source can thus be modelled as a line distribution of longitudinal, axially aligned quadrupoles. However, extension of the following ideas for a source on a cylindrical [84, 85] or conical surface [81] is straightforward; the latter option is particularly attractive, as it allows a representation of the near-field pressure, measured in the irrotational vicinity of the jet.

Harmonic and stochastic variants are discussed in what follows, using, as departure point, the form proposed originally by Crow [70]. While the primary goal of the discussion will be to illustrate the main sound-generating features of turbulent jets, the pertinence of the model will be demonstrated, where appropriate, by comparison with experimental observations.



(a) Compact source, $k_h L = 0.1$



(b) Extended wave-packet source, $k_h L = 5$

Fig. 5: Model time-periodic line sources

3.2 Time-periodic wavepackets (example1.m)

Based on the experimental observations of Mollo-Christensen [68] and Crow & Champagne [18], Crow [70] (see also [45] and [5]) proposed the line-source model,

$$S_{xx}(y) = \exp(ik_h y) \exp\left(\frac{-y^2}{L^2}\right), \quad (34)$$

with k_h the hydrodynamic wavenumber, L the length scale of the wavepacket amplitude envelope, and where an exponential time dependence, $\exp(-i\omega t)$, is implicit. The source is thus a time-periodic, harmonic perturbation, whose amplitude grows and decays as it evolves in the positive x -direction with phase-speed, $c = \omega/k_h$. The number of spatial oscillations that arise between the beginning of perturbation growth and the end of its decay depends on the value of $k_h L$. When this parameter is small the source is compact, as per figure 5(a); when it is large, on the other hand, the source is an extended wavepacket, as per Figure 5(b).⁶

Early sound-source models, such as proposed by Lighthill for instance, were based on an assumption of com-

⁶The figures were generated using the matlab script, example1.m, with the source interval, $y \in [-5, 5]$, discretised with $N = 1001$ equispaced points. Subfigures (a) and (b) are produced by changing the value of k_h appropriately.

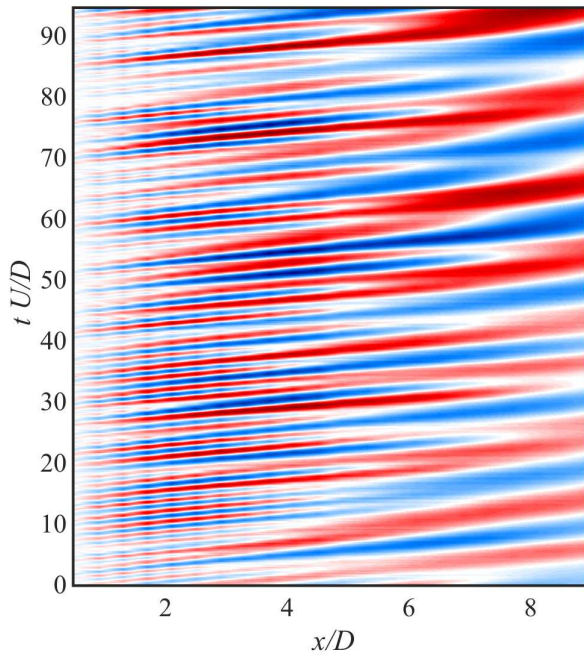


Fig. 6: Axisymmetric hydrodynamic pressure signature of a turbulent jet [14]

compact sources. This was motivated by the 1950s view that turbulence was comprised of disorganised eddies characterised by the integral turbulence scales. Experimental observations since, such as that presented in Figure 6 for instance, show coherent structures in jets to be characterised by large values of $k_h L$, which is consistent with the directivity of jet noise, as we will see in the next section.

3.2.1 Compact and non-compact sources (example2.m)

The solution of Lighthill's wave equation for the farfield sound pressure fluctuation is, in the frequency domain, given by,

$$p(\mathbf{x}, \omega) = \int S(y, \omega) G(\mathbf{x}, y, \omega) dy, \quad (35)$$

where $G(\mathbf{x}, y, \omega)$, the Helmholtz-equation Green's function for an observer situated at \mathbf{x} , regarding a line-source distribution on y , takes the form [45],

$$G(\mathbf{x}, y, \omega) = \frac{e^{ik|\mathbf{x}-y|}}{4\pi|\mathbf{x}-y|}, \quad (36)$$

with $k = \omega/a$ the acoustic wavenumber and a the speed of sound. The sound radiation by the model source is obtained by substituting equations 34 and 36 into equation 35 and performing the integration, which can be done analytically for the far acoustic field in this case, whence the power spectral

density of the sound field is obtained,

$$\langle p(\mathbf{x}, \omega) p^*(\mathbf{x}, \omega) \rangle \approx \frac{1}{16\pi|\mathbf{x}-y|^2} L^2 e^{-\frac{1}{2}k_h^2 L^2 (1-M_c \cos\theta)^2}. \quad (37)$$

The sound fields radiated by the compact and extended-wavepacket sources of figure 6, shown in figure 7, have very different characteristics.⁷ Compact sound sources radiate omnidirectionally, whereas extended wavepackets beam sound energy to low polar angles due to interference between the spatially distributed, convected oscillations.

As equation 37 shows, this beaming effect leads to an exponential dependence of the radiated sound on the modified polar angle, $\Theta = (1 - M_c \cos\theta)^2$. For jets with supersonic convective Mach number, the peak radiation occurs for $\theta = \cos^{-1}(1/M_c)$, which is the Mach angle, associated with Mach waves emitted by wavefronts moving downstream supersonically; this is a feature of the acoustic field of supersonic jets [86, 87], which has been modelled, for instance, by Tam and coworkers [88, 89]. For subsonic convective Mach numbers, the peak radiation is towards the downstream jet angle, $\theta = 0$, and there is exponential decay of sound radiation with increasing polar angle, a behaviour first observed in experiments by Laufer & Yen [90], and later given the term *superdirectivity* by Crighton & Huerre [72]. The superdirectivity of the extended wavepacket source is made clear by plotting the sound pressure level as a function of Θ , as in figure 8, where it is compared with measurements of the axisymmetric part of the sound radiation of a turbulent jet of Mach number, $M = 0.6$, issuing from a round nozzle whose internal boundary layer was tripped and fully turbulent [5]. Sound radiation to low polar angles of this jet is indeed superdirective, indicating that it is driven by an extended source structure characterised by large values of $k_h L$. Such strong directivity of the axisymmetric radiation of subsonic jets has been verified in tests of actual jet engines by Faranosov *et al.* [6]

3.2.2 Acoustic matching (example3.m)

As discussed earlier, not all sound-source activity drives sound waves, and this complicates identification of the acoustically relevant source parameters: a source field may have high amplitude and yet be utterly silent. The notion of acoustic matching, mentioned earlier and which we now consider more closely, helps understand why this is so.

If the observer, at \mathbf{x} , is far from the source ($|\mathbf{x}| \gg |y|$), such that the source can be considered a point, the following farfield assumptions hold: $|\mathbf{x}-y| \approx |\mathbf{x}-y \cos\theta|$, for the phase component of the Green's function that appears in the integrand of equation 35, and $|\mathbf{x}-y| \approx |\mathbf{x}|$, for the decay component associated with the spherical spreading of sound waves.

⁷The source domain, $y \in [-10, 10]$, was discretised with 401 equispaced points. The sound field was computed on a polar arc of radius, $R = 20(M_c * k_h * L)^{-1}$, at 10 degree intervals in the domain, $\theta \in [0, 180]$. The plots in figure 7 can be generated using matlab script example2.m by modifying the parameters M and $k_h L$ accordingly.

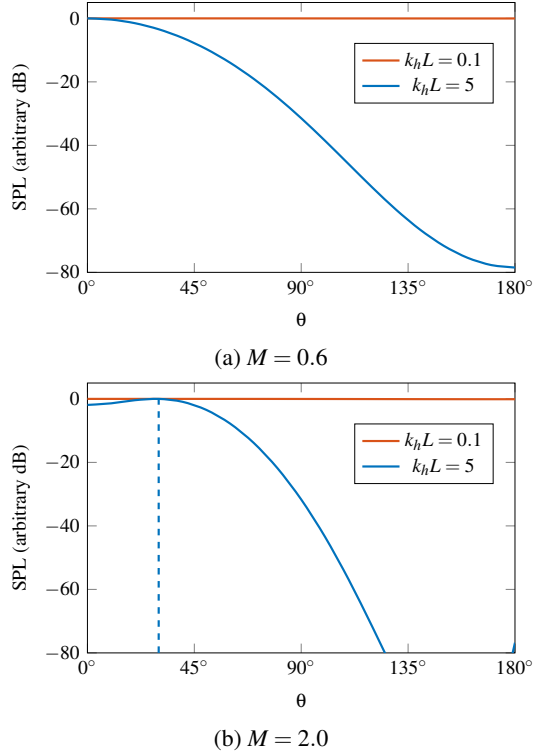


Fig. 7: Sound radiation by a time-periodic, harmonic line-source.

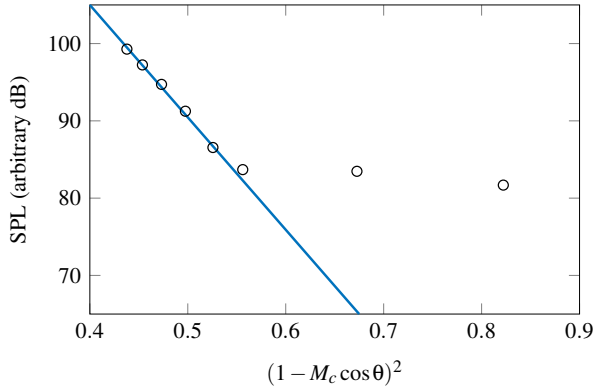


Fig. 8: Superdirectivity. Blue line: extended wavepacket model; Black circles: sound pressure level of the axisymmetric mode at $St=0.2$, from [5]

The Green's function can then be approximated as,

$$G(\mathbf{x}, y, \omega) \approx \frac{1}{4\pi|\mathbf{x}|} e^{ik|\mathbf{x}-y\cos\theta|}, \quad (38)$$

(39)

which has equation 35 take the form,

$$p(\mathbf{x}) = \frac{e^{ik|\mathbf{x}|}}{4\pi|\mathbf{x}|} \int S(y) e^{-iky\cos\theta} dy. \quad (40)$$

This can be recognised as a Fourier transform with modified Fourier modes, $e^{-iky\cos\theta}$: only source modes with non-zero projection onto these can contribute to the farfield sound, i.e.,

$$|k_y| = k \cos \theta, \quad (41)$$

$$\rightarrow \frac{|k_y|}{k} \leq 1, \quad (42)$$

$$\rightarrow \frac{|k_y|}{k_h} \leq M_c, \quad (43)$$

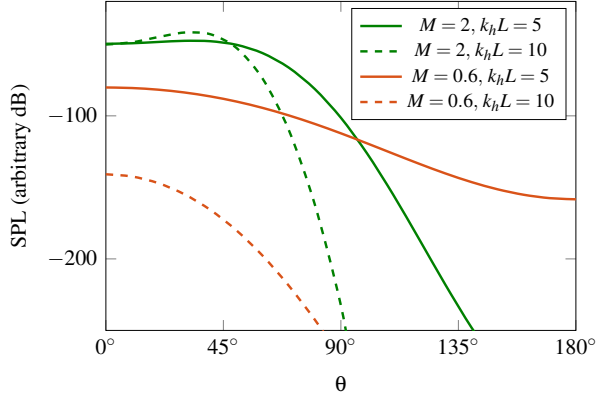
where we have made use of the fact that hydrodynamic and acoustic wavenumbers are related by the convective Mach number, $M_c = k/k_h$. Equation 43 is the acoustic-matching criterion for a line source. It identifies those components of the source field that are active in the generation of propagating sound waves, and can thus be used to understand the acoustic importance of source parameters. Eq. (42) shows that only components with supersonic phase speeds in x are acoustically matched.

The effects of M and $k_h L$ on acoustic emission are shown in figure 9(a). Increasing the Mach number (red to green) clearly enhances the radiated sound levels, as might have been intuitively expected. The effect of $k_h L$ is more subtle, and quite different depending on whether the convective Mach number is subsonic or supersonic. In the former case (red), sound radiation is enhanced if the value of $k_h L$ is decreased (dash-dot to solid), whereas in the latter case the strongest sound levels remain largely unchanged.

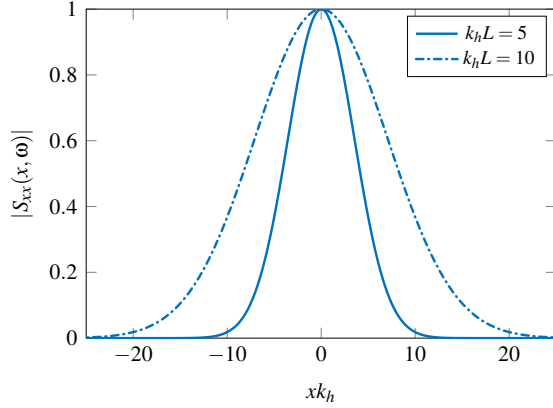
These behaviours can be understood by considering the source structure in wavenumber space, as shown in figure 9(c) (the associated signature in physical space is shown in figure 9(b) for comparison)⁸, where the acoustic-matching criterion of equation 43 is indicated by the vertical lines (red for $M = 0.6$, green for $M = 2$): only source wavenumbers to the left of these (the radiation regime) are acoustically matched. It can be seen how for convectively subsonic wavepackets only a small fraction of the fluctuation energy is acoustically matched, and how decreasing $k_h L$, which narrows (respectively spreads) the source structure in physical (respectively wavenumber) space, considerably increases the energy content in the radiation regime. In the case of convectively supersonic wavepackets, on the other hand, the peak of the wavenumber spectrum already lies in the radiation regime, and so the spreading of the spectrum that occurs when $k_h L$ is decreased does not have so dramatic an effect. The situation of the wavenumber peak in the radiation regime means that the most energetic wavelength of the wavepacket is acoustically matched: it has the same wavelength as the sound field it radiates, something that is visible in numerical simulations, as for example in figure 10 (from [91]). Conversely, the sound field radiated by convectively subsonic jets has wavelength larger than those of their wavepackets, as is also visible in figure 10.

Note that, as discussed in section 2, the integral solution of Lighthill's equation, Eq. 35, once discretised, comprises

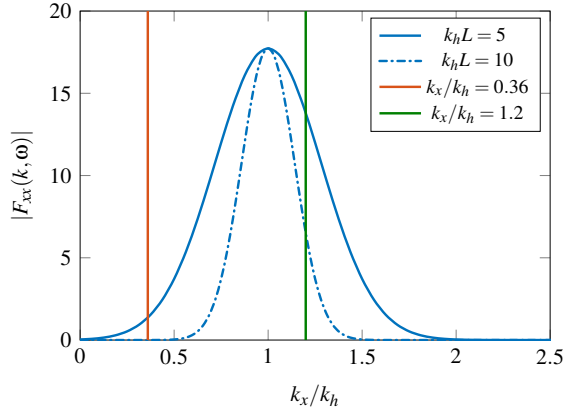
⁸The figures were generated using matlab script example3.m, for a source domain, $y \in [-10, 10]$, discretised with 401 equispaced points.



(a) Effect of M and $k_h L$ on sound radiation



(b) Effect of $k_h L$ on wavepacket amplitude envelope.



(c) Effect of M and $k_h L$ on acoustic matching.

Fig. 9: Acoustic matching

a resolvent, or input-output model. The filtering operation of the integral in Eq. 35 is then embodied in the action of the resolvent matrix on the sound-source vector⁹.

⁹As discussed in section 2, for the specific case of the line-source model, singular-value decomposition of \mathbf{R}_{wave} is problematic, because the natural forcing modes are Fourier modes in y , which are difficult to obtain on account of the inevitable numerical truncation of the source domain. Furthermore, the remedy for this problem, which would involve very long source domains, is incompatible with the requirement that observers be placed in the far field. In the more general case, where streamwise and radial directions are inhomogeneous, SVD of the resolvent operator of eq. (20) allows

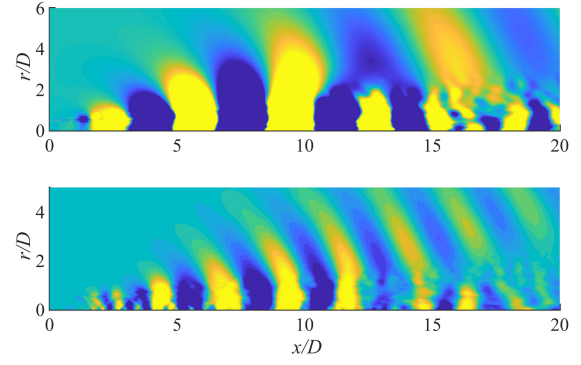


Fig. 10: Axisymmetric wavepackets, at $St = 0.2$, educed from LES data. Top: $M = 0.9$ (courtesy of O. Kaplan); bottom: $M = 1.5$ (from [91]).

3.3 Stochastic wavepackets

The harmonic, time-periodic wavepacket model considered in the previous section, while it serves to illustrate some important features of wavepacket sound radiation, is problematic if we wish to consider the more realistic stochastic source fluctuations characteristic of turbulent jets. In that case, as the fluctuations are described by a stationary random function, the Fourier transform that would provide $S(y, \omega)$,

$$S(y, \omega) = \int_{-\infty}^{\infty} S(y, t) \exp(i\omega t) dt, \quad (44)$$

is ill-defined, as $S(y, t)$ is not square integrable. In order then to consider additional, acoustically relevant, effects associated with source stochasticity, it is necessary to work in terms of PSD and CSD (see section 2.4.1):

$$\langle \hat{p}(\mathbf{x}, \omega) \hat{p}^*(\mathbf{x}, \omega) \rangle = \int_y \int_z \langle S(y, \omega) S^*(z, \omega) \rangle G(y, z, \omega) G^*(y, z, \omega) dy dz, \quad (45)$$

where $\langle \rangle$ denotes ensemble average. The equation shows how the PSD of the sound field is underpinned by the CSD of the source. The double integral that connects the two again involves a filtering of the CSD by the Green's function: the notion of acoustic matching is again central, and it is this that clarifies the acoustic importance of the source parameters, where in this case source stochasticity is accounted for in a statistical manner. Using the resolvent operator and the definitions of section 2.4, eq. (45) can be compactly rewritten, in matrix form, as $\mathbf{P}_{pp} = \mathbf{R}_{SS} \mathbf{R}^H$, where \mathbf{P}_{pp} and \mathbf{P}_{SS} are CSDs of pressure and source, respectively.

the sound-radiation problem to be explored in input-output form, which constitutes a useful means by which to explore, on one hand, the details of acoustic matching, and, on the other, the possibility of low-rank models.

3.3.1 Jitter (example4.m)

The following line-source CSD model has been proposed by Cavalieri & Agarwal [74],

$$\langle S(y, \omega) S^*(z, \omega) \rangle = e^{ik_h(y-z)} e^{\left(-\frac{y^2}{L^2} - \frac{z^2}{L^2}\right)} \times e^{\left(-\frac{(y-z)^2}{L_c^2}\right)}, \quad (46)$$

where y and z are positions on the same line, k_h and L are, as before, respectively, the hydrodynamic wavenumber and the wavepacket amplitude-envelope length scale, and a new parameter, L_c , accounts for stochastic effects. The term $\exp\left(-\frac{(y-z)^2}{L_c^2}\right)$ models loss of coherence between wavepacket source fluctuations separated by distance $|y - z|$, this being due to a desynchronisation of fluctuations that must occur on account of the stochastic nature of the motion of turbulent jets. The effect, which in the time domain is manifest in a spatiotemporal modulation of wavepacket amplitudes (cf. Figure 6(c)), has been termed jitter by Cavalieri *et al.* [73], who demonstrated the central role it plays in determining the acoustic efficiency of wavepackets.

The effect of L_c on the line-source CSD is shown in figure 11¹⁰. Note that the diagonal of the CSD matrix (line from $(-3, 3)$ to $(3, 3)$) represents the PSD of the source, while the off-diagonal terms reflect the level of synchronisation between separated points. For $L_c \ll L$ (Fig 11(a)) the source is highly decorrelated: stochastic effects are such that the wavepacket becomes almost entirely desynchronised as it evolves between adjacent points. This is a behaviour characteristic of the kind of stochastic, uncorrelated eddies of which turbulence was thought to be entirely comprised in the 1950s [92]. In the other extreme, $L_c \gg L$, the wavepacket remains highly synchronised as it evolves in space; its behaviour in this case tends towards that of the time-periodic wavepacket considered earlier, which is perfectly synchronised over its entire extent. The intermediate case, which is closer to what is observed in a real flow, involves a partial desynchronisation of the spatially evolving wavepacket fluctuations: the wavepacket remains largely intact, but jitters.

3.3.2 Acoustic effects (example5.m)

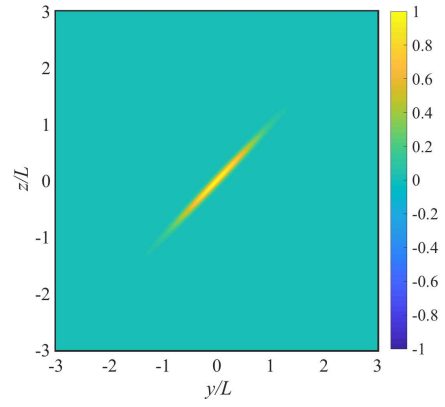
The acoustic implications of the stochastic effects considered above can be explored by substituting eq. (46) into eq. (45) and solving for the farfield PSD, which can again be done analytically, to give [74],

$$\langle p(\mathbf{x}, \omega) p^*(\mathbf{x}, \omega) \rangle \approx \frac{1}{16\pi x^2} L_m L e^{-\frac{1}{2}k_h^2 L_m^2 (1 - M_c \cos \theta)^2}, \quad (47)$$

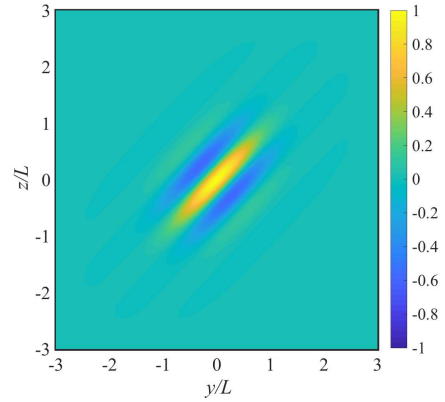
where a modified, effective length, L_m , is given by,

$$L_m^2 = \frac{L^2 L_c^2}{2L^2 + L_c^2}. \quad (48)$$

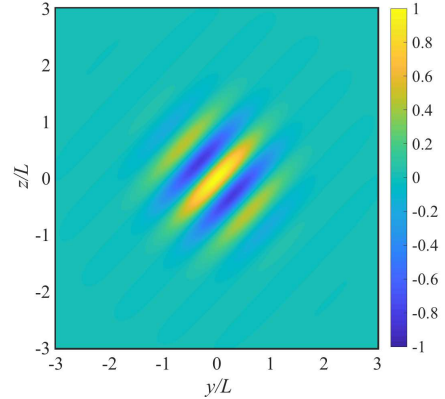
¹⁰The figures were generated using matlab script example4.m, with both dimensions of the two-point source domain, $y_1 \in [-6, 6]$, $z_1 \in [-6, 6]$ discretised with $N = 1201$ points.



(a) $L_c = L/10$



(b) $L_c = L$

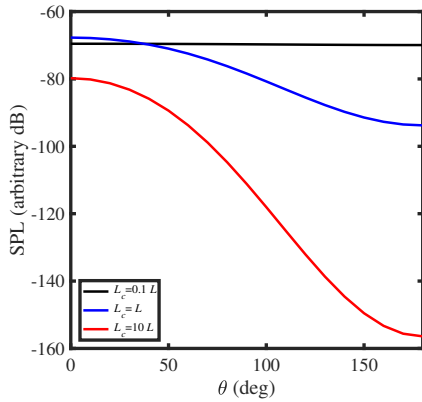


(c) $L_c = 10L$

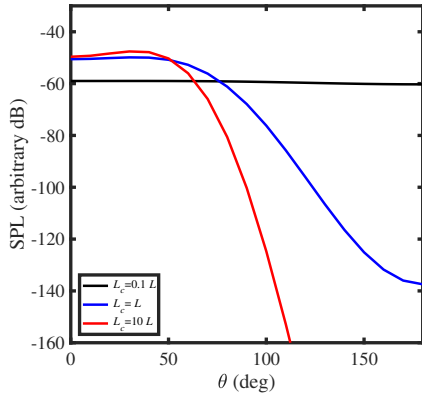
Fig. 11: CSD (real part) of model wavepacket sources, with $k_h L = 5$.

The directivity shape is now characterised by $k_h L_m$. The implications are shown in figure 12 for convectively subsonic and supersonic Mach numbers.¹¹ The following observations can be made. In both subsonic and supersonic cases, the $L_c \ll L$ limit, synonymous with the stochastic-eddy view of

¹¹The figures can be generated using matlab script example5.m, which performs the acoustic computation numerically, using the free-space Green's function. The source domain, $y_1 = z_1 \in [-10, 10]$, was discretised with $N=401$ points and the sound field computed on a polar arc of radius, $R = 20(M_c * k_h * L)^{-1}$, at 10 degree intervals in the domain, $\theta \in [0, 180]$.



(a) $M = 0.6$



(b) $M = 2.0$

Fig. 12: Sound radiation by stochastic model sources

turbulence, leads to omni-directional sound radiation, since the modified length, $L_m \rightarrow 0$ in this case. The effect of near-perfect spatial coherence, $L_c \gg L$, leads to sound radiation such as that produced by the harmonic, time-periodic wavepacket model, as $L_m \rightarrow L$. In the intermediate range, $L_c \sim L$, which is representative of what is observed in real turbulent jets [14, 17], subsonic and supersonic cases differ. In the former case, superdirective radiation is again observed (albeit less marked than in the time-periodic model), but with SPL levels boosted by almost 30dB (three orders of magnitude). It is here that we see the crucial role played by the jitter of subsonically convecting wavepackets: jitter leads to a spatial desynchronisation of flow activity, whence a reduction of cancellation between different regions of the line source, and, consequently, higher sound levels. When the convective Mach number is supersonic, on the other hand, the effect is dramatically different. Jitter has almost no impact on the highest SPL, radiated to low polar angles; its effect is, rather, to boost levels at high emission angles ($\theta > 60^\circ$).

3.3.3 Acoustic matching (example6.m)

This curious behaviour can again be understood by appealing to the notion of acoustic matching. As before, the assumption of farfield radiation allows the PSD of the radi-

ated sound to be written,

$$\langle \hat{p}(\mathbf{x}, \omega) \hat{p}^*(\mathbf{x}, \omega) \rangle = \frac{1}{16\pi^2 R^2} \int_y \int_z \langle S(y, \omega) S^*(z, \omega) \rangle e^{-iyk \cos \theta} e^{izk \cos \theta} dy dz, \quad (49)$$

which we recognise on this occasion as the double Fourier transform of the source CSD and which shows that only CSD wavenumbers satisfying $|k_y| = |k_z| = k \cos \theta$ contribute to the farfield PSD. These are the acoustically matched source wavenumbers, those that drive, or can couple with, propagating sound waves. To obtain sound radiation at some direction θ , these wavenumbers satisfy the inequalities,

$$\frac{|k_y|}{k_h} \leq M_c, \quad (50)$$

$$\frac{|k_z|}{k_h} \leq M_c. \quad (51)$$

With this in mind, it is useful to perform a double Fourier wavenumber transform of the source CSD, two examples of which are shown in figure 13, for $L_c = 10L$ and $L_c = L^{12}$. The squares correspond to the radiation criteria of Eqs. 50 & 51: the red and green squares correspond, respectively, to subsonic and supersonic cases. Only source CSD wavenumbers lying within the radiation squares are acoustically matched and this allows us to better understand the farfield sound features observed in figure 12. For large values of L_c , which correspond to near-time-periodic wavepacket dynamics, the CSD energy lies almost entirely outside the subsonic radiation square, meaning that most of the source activity is uncoupled from the acoustic farfield; the source mostly generates evanescent, nearfield pressure fluctuations. In the case of supersonic convective Mach number, on the other hand, a significant portion of the source CSD lies within the radiation square, explaining the higher acoustic efficiency of the near-time-periodic, supersonically convecting wavepackets.

As the value of L_c is reduced to more realistic values, $L_c = L$, the source CSD gets stretched such that it penetrates into the subsonic radiation square, thereby providing a larger range of acoustically matched wavenumbers. This explains the large difference in radiation levels observed in figure 12(a). A lesser effect is manifest with respect to the supersonic radiation square, as much of the source CSD is already acoustically matched when $L_c \gg L$.

This difference has important implications for jet-noise modelling. It suggests that time-periodic wavepacket solutions of the homogeneous linearised Navier-Stokes equations are sufficient to describe the dominant sound-source activity in supersonic jets provided the initial amplitude is correctly determined—and this is indeed what is observed, in [91] for instance. Whereas in subsonic jets the stochastic

¹²The figures can be generated using matlab script example6.m, which plots the analytical expression for the twice-Fourier-transformed source, as calculated by [74].

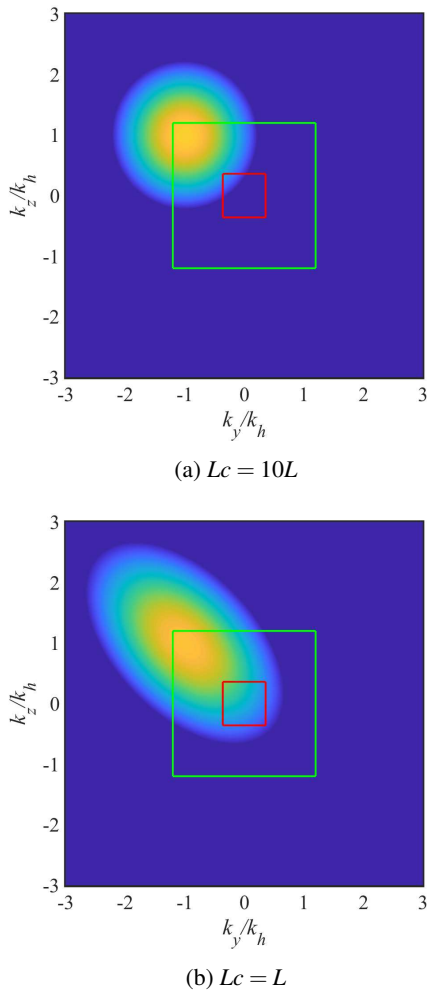


Fig. 13: Source CSD in frequency wavenumber space. Colour scale is logarithmic. Wavenumbers inside the inner red square satisfy $|k_y|, |k_z|/k_h \leq M_c$ for a subsonic jet ($M = 0.6, M_c = 0.36$); wavenumbers inside the outer green square satisfy the same conditions for a supersonic jet ($M = 2, M_c = 1.2$)

jitter of wavepackets is an essential ingredient that must be incorporated in a jet-noise model. In a dynamic linear modelling framework, this can be done by means of a volume-distributed forcing that corresponds to non-linear turbulence and/or wavepacket interactions.

We thus have the following, rather odd-sounding, corollary: the dominant features of supersonic jet-noise may be captured using the Navier-Stokes equations linearised about the time-averaged mean, without requiring what has traditionally been referred to as a source term. All that is required is an initial amplitude, that can be imposed via an upstream boundary condition; convectively subsonic jets, on the other hand, clearly require volume forcing.

Similar to the harmonic, time-periodic case, we note again that the integral solution for the farfield PSD, equation 45, once discretised, takes a resolvent, or input-output form. And again an equivalence exists between the filter-

ing operation by which the Green's function couples acoustically matched stochastic source activity with the acoustic farfield (eq. 45), and the discretised version, which involves a projection of the discretised source CSD into the orthogonal space of input (or forcing) modes, that then connect with the orthogonal space of output (or response) modes via the SVD. The acoustically relevant source activity will thus be contained in the matrix,¹³

$$\mathbf{E} = \Sigma \mathbf{V}^H \mathbf{P}_{ss} \mathbf{V} \Sigma. \quad (52)$$

3.3.4 Spectral Proper Orthogonal Decomposition (example7.m, example8.m)

We now further evaluate the statistics of the stochastic source by taking spectral POD of the CSD in eq 46, using the approach described in section 2.4.2. Figure 14(a) shows eigenspectra for a line-source CSD with $M = 0.6$ & $k_h L = 5$ for three values of the coherence length scale, $L_c = L/10, L$ & $10L$. Figure 14(b) shows the amount of source energy captured as a function of the number of modes retained. The stochastic-eddy source model ($L_c = L/10$), due to its lack of organisation, requires a large number of POD modes for a faithful representation (in terms of source fluctuation energy). The near-perfectly coherent wavepacket model ($L_c = 10L$), on the other hand, can be almost entirely captured with a single POD mode. The intermediate case, which is closer to what is observed in experimental data [14, 17], shows that rank reduction is possible with a small number of modes. The first four modes for this case are shown in figures 15 and 16¹⁴.

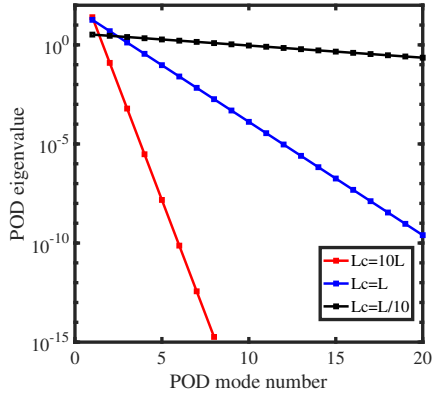
The first POD mode (cf. Figs 15(a) and 16(a)) is what might be referred to as the average wavepacket. The higher-order modes, which involve progressively larger numbers of streamwise oscillations and phase jumps of π (this being due to the orthogonality of the POD basis), reflect the variance of the average source behaviour captured by the first mode. Figure 17 shows how similar behaviour is observed in turbulent jets.

But how much, and what quality, of this variance is required for a given precision in terms of wavepacket jitter and radiated sound? Reconstruction using limited numbers of POD modes provides insight. Figures 18 and 20 show low-rank reconstructions of, respectively, the two-point coherence and the radiated sound¹⁵. The single-mode reconstruction has unit coherence (Fig. 18(a)), like the time-periodic

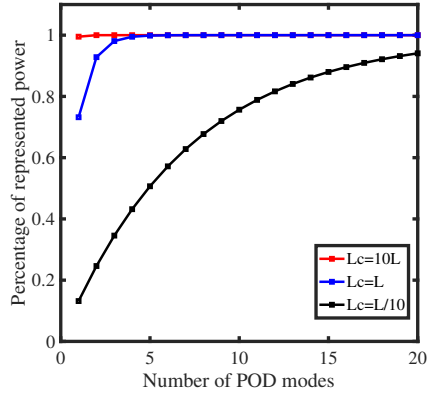
¹³As mentioned in discussing the single-point source, the streamwise-homogeneity of the model source we have considered makes use of this matrix problematic. But in the more general case of inhomogeneous streamwise and radial directions, this matrix is the key to identifying acoustically important source features and modelling them with a reduced-rank system that may be obtained, for instance, by only retaining the forcing modes that truly contribute to the farfield PSD.

¹⁴Figures 14, 15, 16 and 18 can be generated using matlab script example7.m, which performs an eigendecomposition of the source CSD defined on $y_1 = z_1 \in [-10, 10]$ discretised with $N = 400$ points.

¹⁵The figures can be generated using matlab script example8.m, which, following eigendecomposition of the source CSD, computes the sound radiation from low-rank CSD matrices obtained by n -mode POD reconstructions.



(a) POD eigenvalues



(b) Amount of represented power

Fig. 14: SPOD eigenvalues for line-source CSD, S_{SS} .

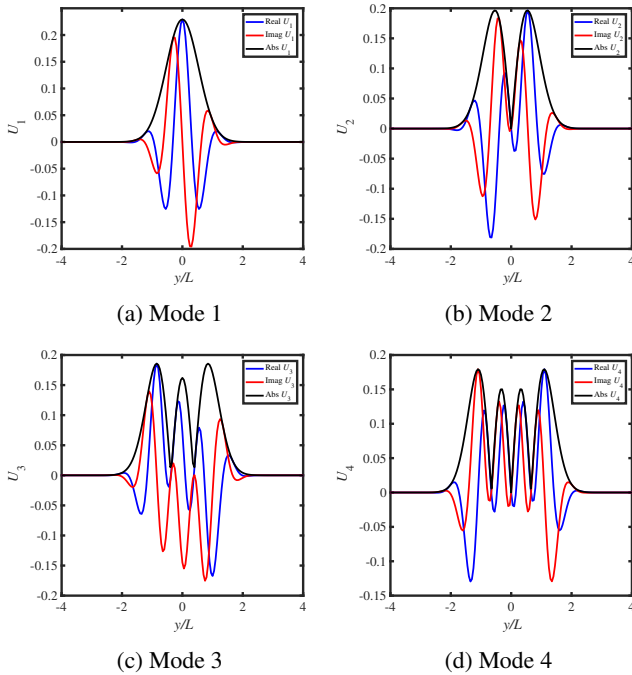


Fig. 15: Source POD modes

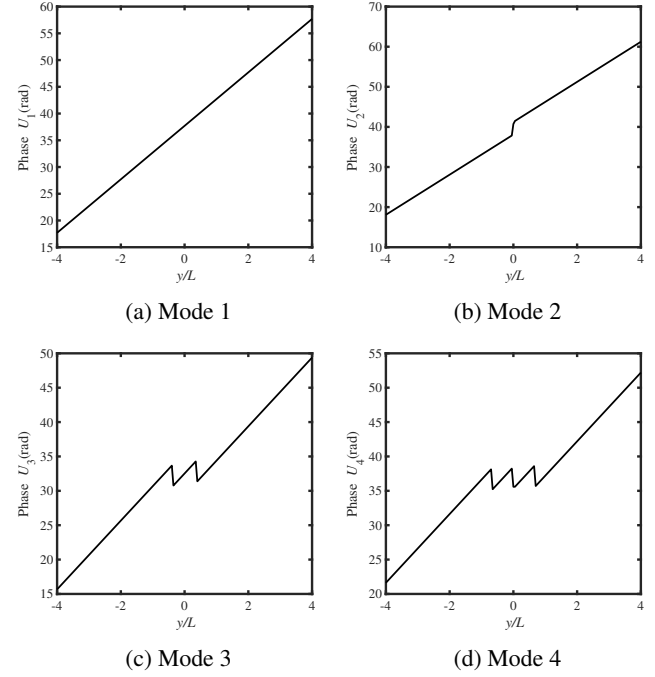


Fig. 16: Phase of POD modes

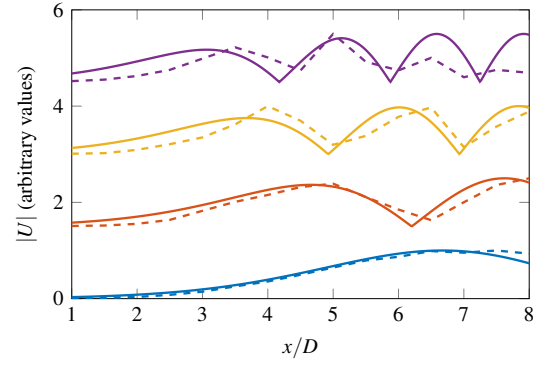


Fig. 17: Comparison of four most energetic modelled (solid lines) and measured (dashed lines) SPOD mode shapes. The first mode is shown on the bottom, and subsequent modes are plotted with the upper curves. SPOD modes taken from the measurements of Jaunet *et al.* [17], radially integrated to obtain an equivalent stochastic line source.

model considered earlier, and captures, as a consequence, only a small fraction of the radiated sound for the subsonic case (Fig. 20(a)). With three modes (Fig. 18(c)), the coherence in the region where the wavepacket has significant amplitude ($-2 < y/L < 2$) is similar to that of the complete CSD (Fig. 18(d)), and the dominant sound radiation (Fig. 20(a)), to low polar angles is, as a consequence, almost perfectly captured; we can say that most of wave-packet jitter has been captured by superposition of the three leading SPOD modes. Such reconstruction of source coherence is similar to what is obtained using experimental data: figure 19 shows similar reduced-rank reconstructions based on pressure fluctuations measured in the nearfield of a subsonic turbulent jet [14].

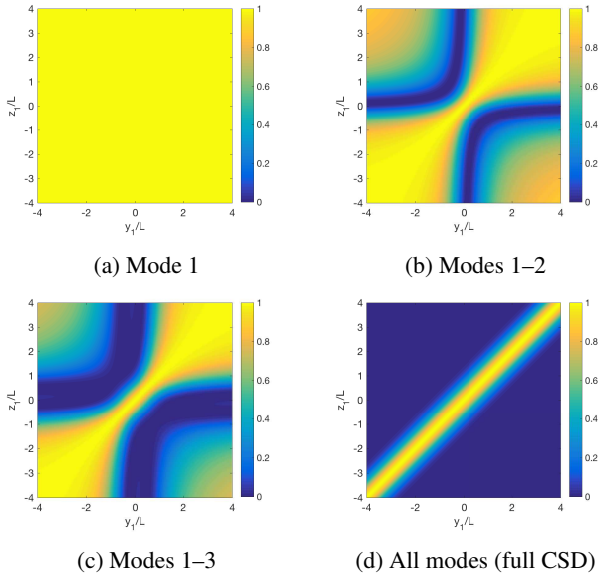


Fig. 18: Two-point coherence of reconstructions of the model source CSD

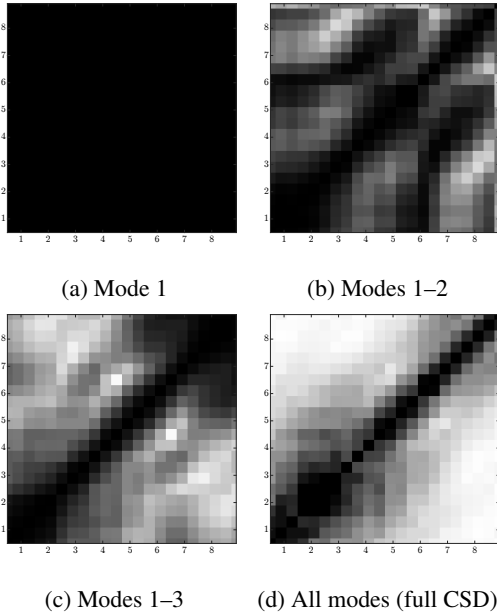


Fig. 19: Two-point coherence of reconstructions of measured nearfield pressure CSD, from Breakey *et al.* [14]. White represents zero and black shows unit coherence.

The supersonic case is again different, for reasons already evoked: the results of figure 20(b) show that a single POD mode, with its unit coherence, is sufficient to describe the dominant sound radiation.

These results, obtained using a simplified model source, highlight something that has been observed in the analysis of subsonic jet noise: while SPOD provides an optimal modal decomposition of the turbulent kinetic energy, the leading SPOD modes often have a marginal contribution to the radiated sound, and superposition of a larger number of modes is

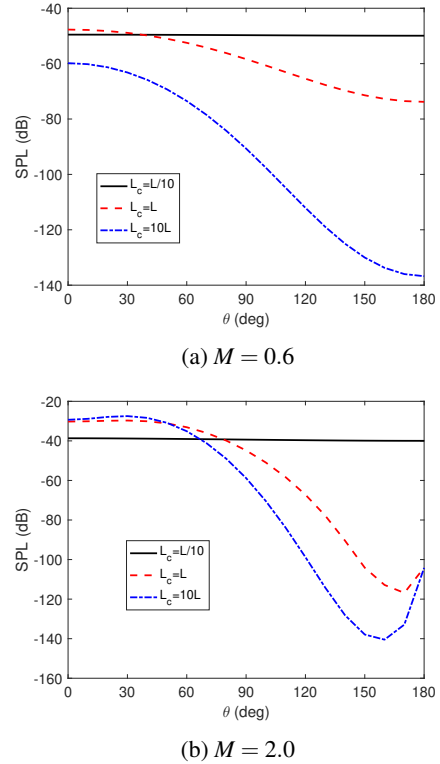


Fig. 20: Sound radiation by stochastic model sources, decomposed into POD modes. Results for $k_h L = 5$ and $L_c = L$.

required to obtain sound radiation close to what is observed in the acoustic field. This has been observed by Freund & Colonius [93] using POD (without going to the frequency domain), and, more recently, by Towne *et al.* [94] with SPOD taken for a Mach 0.9 jet.

4 Dynamics of wavepackets

While the kinematic model presented in section 3 is intended to represent idealised wavepacket shapes in jets, dynamically, these wavepackets arise from the instability of jet flows. These unstable dynamics may be characterised using linear analysis. Accepting the usefulness of the line source hypothesis for the conceptual investigation of jet acoustics, we now employ a one-dimensional dynamical law for the modelling of near-field fluctuations.

The Ginzburg–Landau equation provides a classical model problem for instability-driven flow dynamics. In its linear form, it is written as

$$\partial_t q + U \partial_x q - \gamma \partial_{xx} q - \mu q = 0. \quad (53)$$

The complex-valued function $q(x, t)$, defined over $x \in (-\infty, \infty)$ and $t \in [0, \infty)$, is considered to represent flow fluctuations; its real part can be identified with any observable fluctuation quantity, as for example Lighthill source terms. The first three terms in (53) represent one-dimensional convection and diffusion, whereas the last term allows the sta-

bility characteristics to be controlled according to our needs. Assuming for the moment that all parameters are constant in x , one can insert normal-mode solutions, $q(x,t) = \hat{q}e^{ikx - i\omega t}$, into (53). The dispersion relation is then readily obtained as,

$$\omega = kU - i\gamma k^2 + i\mu. \quad (54)$$

Instability, characterised by $\omega_i > 0$ for $k \in \mathbb{R}$, can only be achieved if (i) U is complex, (ii) the diffusion coefficient γ_r is negative, or (iii) μ_r is positive. The first two choices are difficult to justify as an analogy for the Navier–Stokes equations; it is therefore convenient to choose $U \in \mathbb{R}$, $\gamma_r > 0$ and $\mu \in \mathbb{R}$. The dispersion relation (54) shows that such a system is stable for $\mu < 0$ and unstable for $\mu > 0$.

The group velocity of oscillations is found from (54) to be,

$$\frac{\partial \omega}{\partial k} = U - 2i\gamma k. \quad (55)$$

Dispersion, characterised by a dependence of the real part of the group velocity on the wavenumber, is therefore governed by the imaginary part of γ ; for $\gamma \in \mathbb{R}$, the linear Ginzburg–Landau equation is non-dispersive. In what follows, we fix $U = 1$ and $\gamma = (1 - i)/10$.

The absolute frequency/wavenumber pair, which evolves at zero group velocity, is found from (54,55) to be given by,

$$\omega_0 = i \left(\mu - \frac{U^2}{4\gamma} \right), \quad k_0 = -\frac{iU}{2\gamma}. \quad (56)$$

4.1 Modal stability properties of the Ginzburg–Landau system

The Ginzburg–Landau equation must be calibrated, via the tuning parameter, μ , for our purpose to use it as a model problem for wavepacket dynamics in a jet. This is done by prescribing a streamwise variation for μ , such that the principal stability properties of a typical jet are qualitatively reproduced. We start with a *local* analysis of these properties, in order to motivate the choice of $\mu(x)$, and then describe the *global* stability behaviour in terms of temporal eigenmodes. In a local analysis, it is assumed that propagating waves at any given station x evolve according to the dispersion relation (54), with the local parameter values, as if these were constant in an infinite domain. In the context of flow problems, this is known as the *locally parallel flow assumption*. A global analysis of the Ginzburg–Landau equation fully accounts for the effects of streamwise parameter variations on the evolution of waves.

4.1.1 Local stability and the choice of $\mu(x)$ (example9.m)

The linear Ginzburg–Landau equation has often been used as a model for the study of instability in spatially developing shear flows [95, 29]. The spatial variation of local

stability characteristics of a given flow, in particular the maximum temporal growth rate, ω_i^{max} , over all values of k at a streamwise station, x , can be reproduced in the Ginzburg–Landau model by a prescribed variation, $\mu(x)$. Two particular variations have been widely used in the literature: a parabolic function, $\mu(x) = -ax^2 + b$, with $a > 0$ and defined over $x \in (-\infty, \infty)$, yields a system that is locally stable to both sides far from the origin, and, depending on the parameter b , may present a locally unstable region around $x = 0$. A linearly decaying variation, $\mu(x) = -ax + b$, with $(a, b) > 0$ and defined over the interval, $x \in [0, \infty)$, defines a system that is locally unstable at the boundary, $x = 0$, but in which the maximum growth rate decays linearly in x , such that local stability is reached at a distance, $x_s = b/a$.

A parabolic variation of $\mu(x)$ therefore provides a model for a flow problem characterised by a pocket of (potentially absolute) local instability embedded in a stable environment [95], as for instance a bluff-body wake. Recently, such models have been used by Bagheri et al. [29] and Towne et al. [37] for illustrations of instability dynamics. In the present paper, we seek a Ginzburg–Landau system that mimics the dynamics of jets; a *linearly decaying* variation of $\mu(x)$ is appropriate in this case. Within the potential core, for as long as the shear-layer thickness, θ , is small compared to the nozzle diameter, the local maximum growth rate, ω_i^{max} , is proportional to the inverse of θ [96]. Since θ grows linearly in x in a turbulent jet [97], ω_i^{max} decays monotonously in the downstream direction.

In what follows, we prescribe

$$\mu(x) = A(1 - x/10), \quad A > 0, \quad (57)$$

such that the system is locally unstable for $x < 10$, and locally stable for $x > 10$. With the choice, $U = 1$ and $\gamma = (1 - i)/10$, absolute instability at the upstream boundary arises when A is greater than 1.25; with lower values of A , the system is only convectively unstable over the interval, $0 \leq x < 10$. In jets, absolute instability only occurs in the presence of significant density differences [98]. The local analysis examples in this section are limited to values, $A \leq 1.25$.

For three values, $A = 0.6, 1$ and 1.25 , the spatial variation of the growth rate, $-k_i$, is traced in Figure 21a as a function of x , for a constant frequency value, $\omega = 1$. Figures 21b, c show the corresponding real parts of the wavenumber k , and of the phase velocity $c = \omega/k$. Real and imaginary parts are denoted by subscripts r and i from here on. Two branches, k^+ and k^- , are obtained for each parameter setting: the k^+ branch (shown in red) describes downstream-propagating waves, while the k^- branch (shown in blue) describes upstream-propagating waves emanating from a source placed inside the domain (see Huerre [95] for the definition of k^+ and k^- branches based on the impulse response of the system). It is seen in figure 21a that higher values of A lead to higher growth rates of the k^+ branch near the upstream boundary¹⁶, and overall stronger streamwise variations of all curves. While the influence of A on the real part

¹⁶With the normal mode convention $\exp(ikx - i\omega t)$, one has a spatial de-

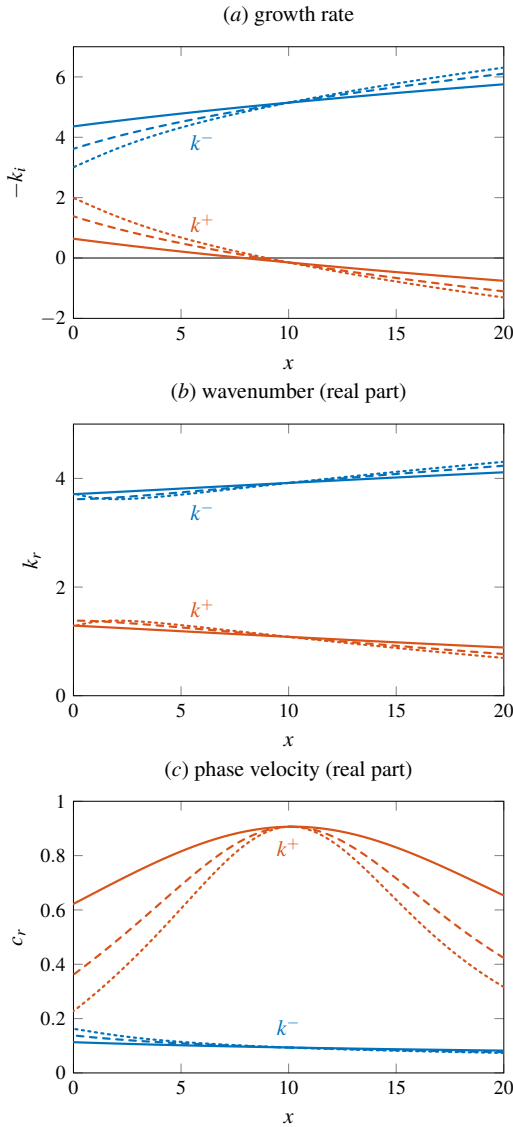


Fig. 21: Local spatial instability branches of the Ginzburg–Landau equation, for $\omega = 1$. Solid lines: $A = 0.6$; dashed lines: $A = 1$; dotted lines: $A = 1.25$.

of the wavenumber seems to be modest, the phase velocity of the k^+ branch is quite strongly affected.

The spatial growth rate, $-k_i$ of the k^+ branch decays monotonously in x at all values of ω and $A \leq 1.25$, and in the case, $\omega = 1$ and $A = 0.6$ this decay is approximately linear. Based on this local analysis of spatial amplitude growth, a first-order estimate for the amplitude envelope of an instability wave, developing in response to harmonic forcing at the upstream boundary, would predict a *Gaussian* shape, with its maximum at the location where $k_i^+ = 0$, and with an envelope length that depends on the rate of streamwise decay of k_i^+ . This is precisely the type of harmonic source term

pendence of $\exp(ik_r x - i\omega t) \exp(-k_i x)$. Negative k_i indicates thus spatial growth for increasing x , and thus a spatial instability for the k^+ branch. On the other hand, the k^- branch is an upstream-travelling wave, and thus its spatial growth rate, in the direction of propagation, would be k_i . This mode thus decays in the direction of propagation for the parameters chosen here.

distributions discussed in section 3.2.

4.1.2 Global instability eigenmodes of the Ginzburg–Landau system

Global eigenvalues, ω_n , and associated eigenfunctions, $q_n(x)$, are defined as solutions of the eigenvalue problem,

$$\omega_n q_n(x) = -i[U\partial_x - \gamma\partial_{xx} - \mu(x)]q_n(x), \quad (58)$$

$$q_n(0) = 0, \quad (59)$$

derived from the Ginzburg–Landau equation (53) with the *ansatz*, $q(x,t) = q_n(x)e^{-i\omega_n t}$. For the particular case of a linearly decaying parameter, $\mu(x) = A(1 - x/10)$, the eigenvalue solutions on the semi-infinite domain, $x \in [0, \infty)$ are known analytically [99] to be given by,

$$\omega_n = i \left\{ A - \frac{U^2}{4\gamma} + \gamma^{\frac{1}{3}} \left(\frac{A}{10} \right)^{\frac{2}{3}} \zeta_n \right\}, \quad (60)$$

where ζ_n denotes the countable set of roots of the Airy function. The largest growth rate among this set of eigenvalues is found for ω_1 , generated with $\zeta_1 \approx -2.338$; its variation with A is shown in figure 22a. Global instability arises for $A > 1.6$, and the spectrum for this critical value is displayed in figure 22b: red symbols mark the exact values according to (60), whereas black circles represent a *numerical* approximate solution of the eigenvalue problem (58), computed with the routine, *example10.m*.

The interval $x \in [0, 20]$ is discretised with $N = 200$ points, given by the roots of the Chebyshev polynomial of order 200; the *Chebyshev collocation method* that is used for the discrete representation of derivatives in x yields spectral-like accuracy [100]. As the infinite domain of the original problem (58) needs to be truncated for the numerical representation, Dirichlet boundary conditions, $q_n(x) = 0$, are imposed at both boundaries, $x = 0$ and 20. It is found that the seven eigenvalues with highest temporal growth rates, which dominate the long-time dynamics, are accurately recovered in the numerical solution. Subsequent eigenvalues differ between the continuous and the discrete systems; this is due to spurious upstream feedback, generated by the artificial downstream boundary condition. The same effect is observed in global eigenmode calculations of jet flows in truncated domains [101].

The numerically computed eigenfunction, $q_1(x)$, corresponding to the marginally stable eigenvalue, ω_1 for $A = 1.6$, is displayed in figure 22c. Its real and imaginary parts represent snapshots of the wavepacket, $\Re[q_1 \exp(-i\omega_1 t)]$, at two instances separated by a temporal phase difference, $\pi/2$. The amplitude envelope, $|q_1(x)|$, approximately of Gaussian shape, has zero group velocity, i.e. it remains at its location at all times. In this particular case of marginal stability, its magnitude is also constant in time. The model flow fluctuation, q , forms waves that travel downstream, with positive phase velocity, under this envelope function.

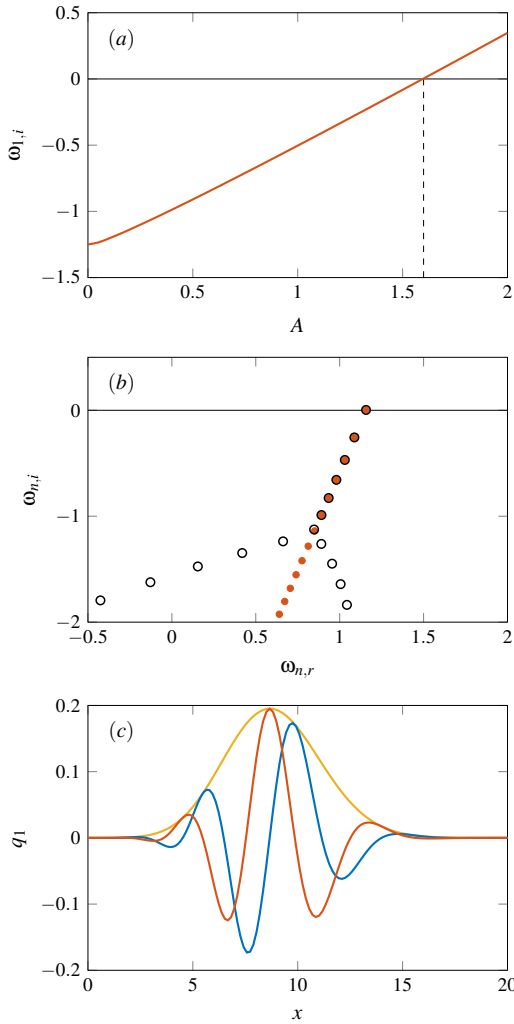


Fig. 22: Global stability spectra of the Ginzburg–Landau equation (58). *a*) Maximum growth rate $\omega_{1,i}$ as a function of A . *b*) Eigenvalue spectrum for the marginally stable case $A = 1.6$, (●) exact eigenvalues of the continuous problem, (○) numerical eigenvalues of the discretised problem. *c*) Eigenfunction $q_1(x)$ associated with the marginally stable eigenvalue for $A = 1.6$; (—) real part, (—) imaginary part, (—) modulus.

Linear global instability is typically associated with the onset of nonlinear limit-cycle oscillations [52], as for instance the von Kármán vortex street in a cylinder wake [102]. In this case, any initial condition, without further excitation, would give rise to a global instability that saturates due to non-linear effects; this is referred to as a self-excited oscillation, or as *oscillator* behaviour [52]. In jets, such behaviour is only observed in the laminar regime, when the density of the jet fluid is significantly lower than the ambient density [103, 104]. Weakly stable eigenmodes of a different nature may occur in turbulent jet mean flows [105], without however leading to limit-cycle behaviour. Globally unstable settings of the Ginzburg–Landau model ($A > 1.6$) are therefore excluded from this paper, and global stability of a linear system is a strict requirement for the following analysis of

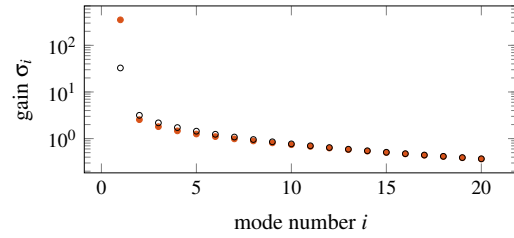


Fig. 23: Resolvent gain values of the Ginzburg–Landau system for $\omega = 1$: (●) $A = 1$, (○) $A = 0.6$.

its response to sustained forcing, where we examine the case of an *amplifier* flow: even though there is global stability, external forcing may be significantly amplified.

4.2 Global response of the Ginzburg–Landau system to harmonic forcing

A harmonic forcing term, $f(x, t) = \hat{f}(x)e^{-i\omega t}$, is now added to the right-hand side of the Ginzburg–Landau equation (53), in analogy to the separation of nonlinear terms in the Navier–Stokes system, discussed in section 2.2. In the frequency domain, with the definition of a Fourier transform and its inverse given by eqs. (5) and (6), the input-output relation between the forcing, $\hat{f}(x)$, and the associated linear response, $\hat{q}(x)$, in the asymptotic limit, $t \rightarrow \infty$, has the form,

$$\hat{q}(x) = (-i\omega + U\partial_x - \gamma\partial_{xx} - \mu)^{-1}\hat{f}(x), \quad (61)$$

with boundary conditions, $\hat{q}(0) = \hat{q}(20) = 0$, at both ends of the domain, $x \in [0, 20]$. After spatial discretisation, and without imposing any restrictions on the forcing support and the output selection ($\mathbf{B} = \mathbf{C} = \mathbf{I}$ in the state-space form of eqs. 17 and 18), the matrix-vector form (19) of the Ginzburg–Landau input-output system is recovered. The singular value decomposition (20) of the resolvent matrix, \mathbf{R} , is easily constructed¹⁷.

The gain values, σ_i , corresponding to $A = 1$ and a frequency, $\omega = 1$, arranged in descending order as explained in Section 2.3, are plotted in Figure 23 as red symbols. A strong separation, by more than two orders of magnitude, between the first and all subsequent σ_i is observed in this case. For comparison, $A = 0.6$ leads to a gain separation by only a factor, $\sigma_1/\sigma_2 \approx 10$ (black symbols).

Forcing and associated response structures of the first four singular modes, obtained for $A = 1$, are shown in figure 24. The optimal forcing (mode 1) is concentrated near the upstream boundary: forcing in this region optimally exploits the spatial instability of the k^+ mode, as given in figure 21*b* (red dashed line). Very near the boundary, the Dirichlet condition, $\hat{q}(0) = 0$, is felt via the effect of diffusion, such that forcing is not efficient. The optimal response wavepacket has

¹⁷This computation is carried out in example11.m. The same discretisation as in example10.m is used. Note that the Chebyshev point distribution leads to non-uniform weights, which are accounted for according to the equations provided in [50, 38, 51]. Weights were obtained considering Clenshaw-Curtis quadrature [106].

a nearly Gaussian bell shape, with its maximum at $x = 8.55$; this compares well with the station, $x = 8.73$ where the local k^+ mode becomes stable for $\omega = 1$. In particular, the optimal response mode in figure 24b should be compared to the kinematic model wavepackets in figure 5. The dynamic model provided by the Ginzburg–Landau system, with a linear variation of $\mu(x)$ on a half-infinite domain, is indeed fully consistent with the kinematic model discussed in section 3.2, which has been demonstrated to represent a number of trends seen in jet experiments. Note also that the optimal response of the Ginzburg–Landau equation has the features of the leading SPOD mode of a turbulent jet shown in figure 2(b), with amplification, saturation and decay of a coherent wave.

The second response mode, shown in figure 24d, must be orthogonal to the first by construction. The most efficient way to achieve this is to create a structure consisting of two symmetric lobes, one of which is in phase opposition with the first response wavepacket. Incidentally, the forcing that is required for such a response structure (figure 24c) is very similar in shape to the first response mode. The same pattern is repeated in subsequent resolvent modes: forcing and response structures feature an increasing number of lobes in phase opposition, the forcing of one mode mirroring the shape of the previous response. Note that only the optimal mode fully thrives on the k^+ instability dynamics for achieving strong energy gain; once this mechanism is exploited, all suboptimal modes only involve an alternating generation and cancellation of the k^+ wave, with gain values of order unity. The very same shapes of suboptimal orthogonal flow response structures have been shown to arise as spectral POD modes in the kinematic model discussion of section 3.3 (see figure 15).

While the optimal resolvent mode of the Ginzburg–Landau model is largely analogous to that found in jet flows, which also present a single unstable local k^+ branch that provides the most potent mechanism for energy gain [39,38,51], important differences between the two arise from the fact that the Ginzburg–Landau system only permits one k^+ solution. Jet flows, due to their transverse spatial dimensions, possess an infinite number of stable non-orthogonal k^+ local eigenmodes, which can combine to create transient spatial growth via the Orr mechanism [107]. This mechanism provides an alternative means of generating energy gain, and may in certain cases dominate the suboptimal resolvent modes in jets [38,51]. The one-dimensional Ginzburg–Landau model is not capable of reproducing such dynamics.

4.3 Global response of the Ginzburg–Landau system to stochastic forcing

In analogy to the kinematic description of stochastically jittering wavepackets in section 3.3, we now consider the response of the Ginzburg–Landau system to stochastic forcing input. The Gaussian factor in eq. (34), which carries over to the kinematic CSD model (46), is produced by the resolvent of the dynamic model in a deterministic way. The stochasticity that is contained in the coherence decay term in

eq. (46), however, must be inherited from stochastic forcing in the Ginzburg–Landau model. We prescribe the CSD of stochastic forcing input in non-discrete form as,

$$\langle f(x_1, \omega) f^*(x_2, \omega) \rangle = e^{ik_h(x_1 - x_2)} e^{-\frac{(x_1 - x_2)^2}{L_c^2}}, \quad (62)$$

and obtain the matrix \mathbf{P}_{ff} by evaluating that forcing CSD at discrete x -positions. The corresponding response CSD is then found directly from the relation (31) via the resolvent operator in eq. (61). Fixing $k_h = 1$, and varying the coherence variance between $L_c = 0.1$ (weak spatial coherence) and 10 (strong spatial coherence), three cases are presented in figure 25. Values $\omega = 1$ and $A = 0.6$ are used in these examples.¹⁸

It appears from the plots in figure 25 that the coherence of the forcing has little effect on the response statistics; only slight differences can be spotted at the tails of the response CSD. A finer analysis of the differences between high- and low-coherence forcing is based on an inspection of the first four SPOD modes, found as the leading eigenvectors of the response CSD. Only the two extreme cases, $L_c = 0.1$ and 10, are represented in figure 26.¹⁹ Black dotted lines in the plots of the $L_c = 0.1$ results indicate the amplitude envelope of the corresponding resolvent response modes for $A = 0.6$. It is seen that the stochastic response to weakly coherent forcing, indeed very close to the assumption of ‘spatially white noise’, reproduces with high accuracy the resolvent response modes obtained for *harmonic* forcing, as predicted in section 2.4.3. Strongly coherent forcing, in contrast, only reproduces the optimal resolvent response mode; subsequent SPOD modes differ significantly from the resolvent suboptimal. This is due to the dominance of the leading response. Since the gain of the first mode, σ_1 , is ten times larger than those of the higher modes, it tends to dominate the response CSD even if the forcing is not white, as discussed in section 2.5.

Several studies have shown that jets do exhibit a strong separation between the optimal gain value and suboptimal ones, in a band of Strouhal numbers around $St \approx 0.4$ (the ‘preferred mode’) [39,63,49,36,37,38,51]. A comparison between an experimentally measured leading SPOD mode and the optimal resolvent mode, at $St = 0.4$ in a turbulent jet at $Ma = 0.4$ and $Re = 460000$, is given in figure 27. While the optimal resolvent mode, computed on the experimental mean flow, very well reproduces the first SPOD mode, no good matching is obtained for suboptimal structures [51]. The above discussion of figure 26 suggests that high coherence in the Reynolds stress fluctuations may explain this observation.

We see that the response of the Ginzburg–Landau equation to stochastic forcing leads to a jittering wave-packet, with features similar to those of the kinematic model described in section 3.3.1. In the next section, we couple

¹⁸These results can be obtained using example12.m with the above choice of parameters.

¹⁹These results were obtained with the script example13.m. A numerical interval $x \in [0, 30]$ is chosen for the calculations, in order to fully resolve the SPOD structures at least in the low-coherence case.

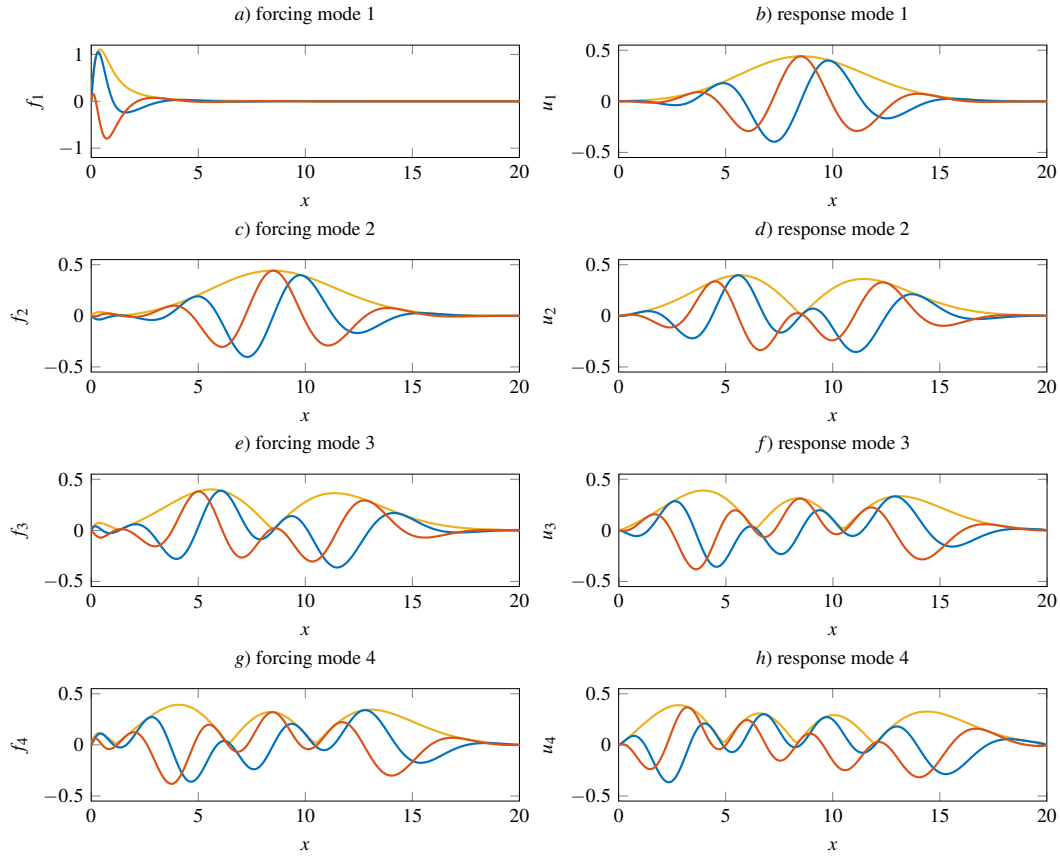


Fig. 24: The first four resolvent modes of the forced Ginzburg–Landau system, for $\omega = 1$ and $A = 1$. Legend: (—) real part, (—) imaginary part, (—) modulus.

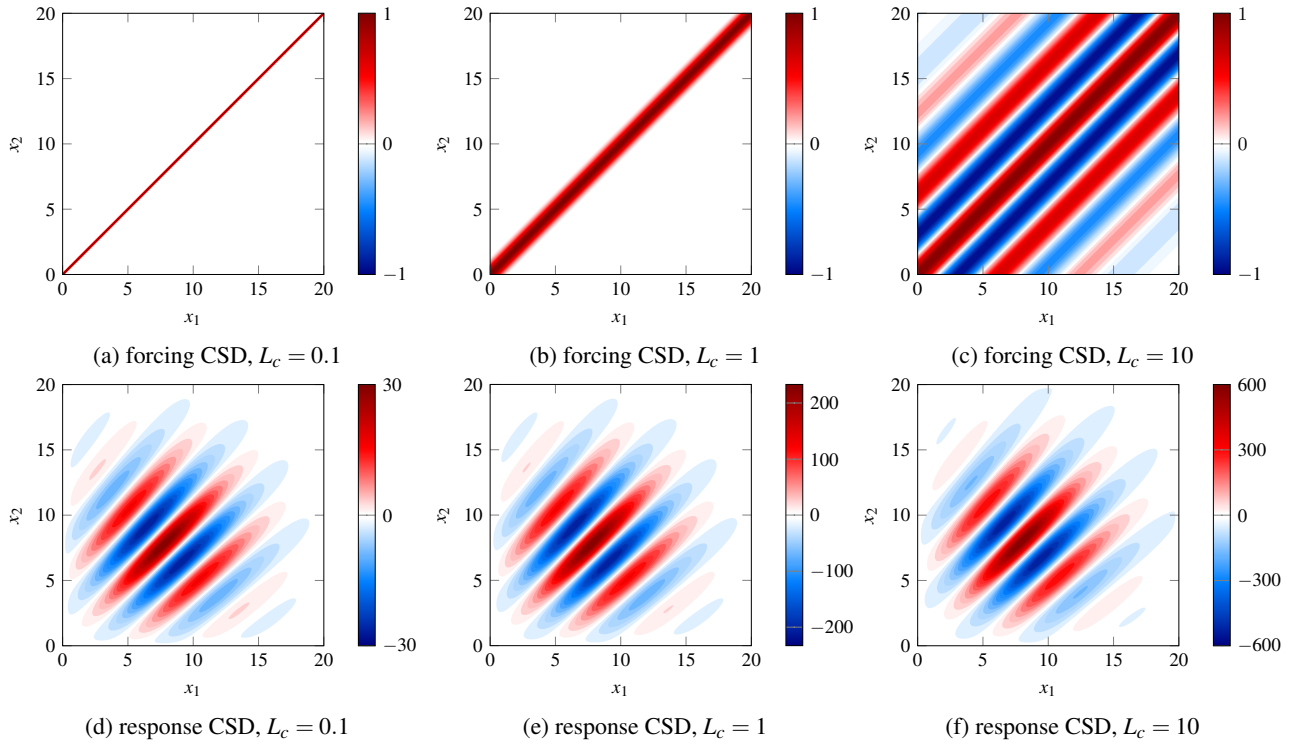


Fig. 25: Forcing and response CSDs (real part) of the stochastically forced Ginzburg–Landau system, for parameters $A = 0.6$, $\omega = 1$, $k_h = 1$ and L_c as indicated.

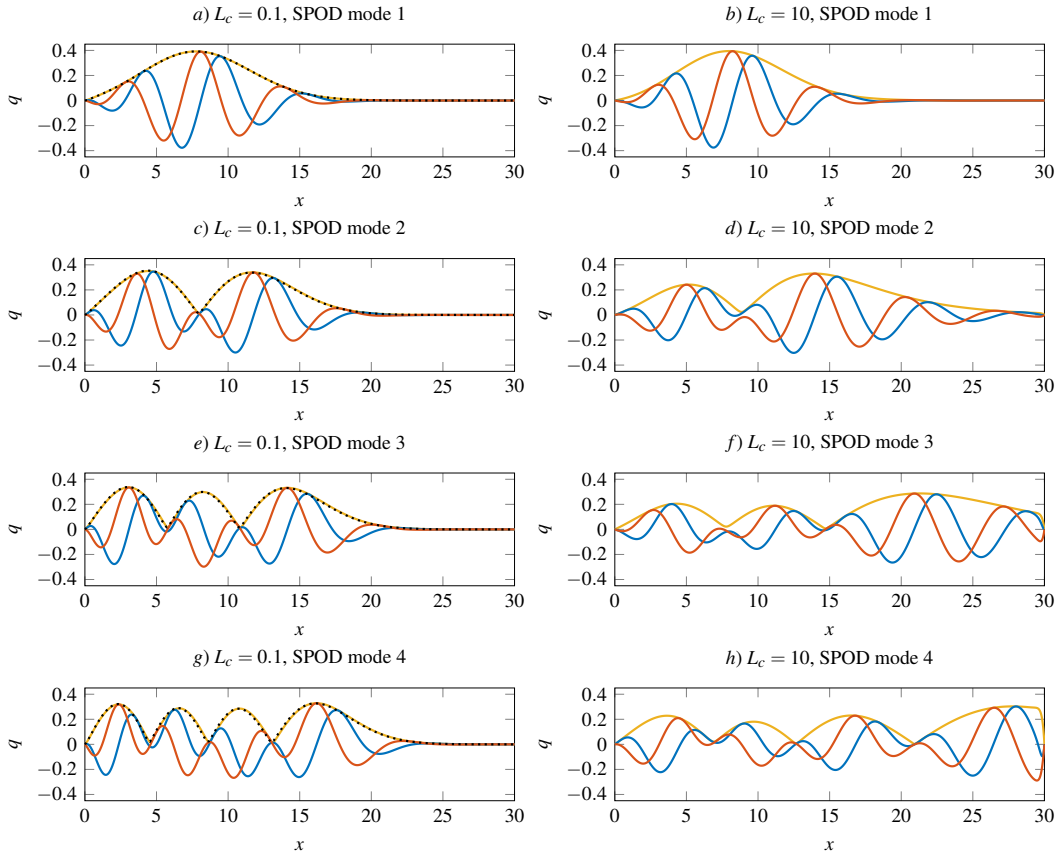


Fig. 26: The first four SPOD modes of the stochastically forced Ginzburg–Landau system, for $\omega = 1$ and $A = 0.6$. Left column: low-coherence case $L_c = 0.1$, right column: high-coherence case $L_c = 10$. Legend: (—) real part, (—) imaginary part, (—) modulus. Dotted black lines represent the modulus of the corresponding resolvent response modes.

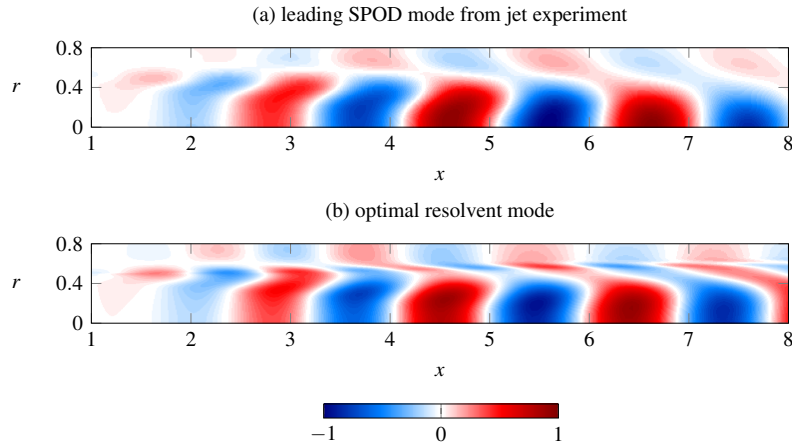


Fig. 27: First SPOD mode (measured) and first resolvent mode (computed) in a turbulent jet at $St = 0.4$, $Ma = 0.4$ and $Re = 460000$. Results show the real part of axial velocity fluctuations. Made with data from [51].

the Ginzburg–Landau and wave equations, building another model problem that allows us to explore how dynamic features studied in this section couple with the acoustic field.

5 Extending dynamic models to the acoustic field

5.1 Model problem

We here combine the model problems of sections 3 and 4 in order to have a simplified view of the coupling between wavepacket dynamics and sound radiation. The basic idea is

to consider the wave equation forced by a line source, $q(x, t)$,

$$\Delta p - \frac{1}{c_0^2} \frac{\partial^2 p}{\partial t^2} = q(x, t), \quad (63)$$

which, in turn, comes from a forced Ginzburg-Landau equation,

$$\partial_t q + U \partial_x q - \gamma \partial_{xx} q - \mu q = f. \quad (64)$$

This coupled problem is akin to hybrid methods in aeroacoustics, where a flow solution is obtained, sometimes assuming incompressible flow, and subsequently used to build Lighthill's stress tensor, which in turn can be used to obtain the radiated sound field. Such methods have been reviewed by Colonius & Lele [108] and Wang *et al.* [109]. However, since a compressible Navier-Stokes computation leads directly to the radiated sound, a resolvent analysis using the compressible linearised operator directly relates non-linear terms to the radiated sound once an observation operator, \mathbf{C} , is chosen to take the radiated sound as the output, as discussed in section 2.2. Garnaud *et al.* [48] and Jeun *et al.* [49] use this approach for the analysis of sound radiation of subsonic and supersonic jets. We here use the coupled problem for its simplicity, with two equations whose inputs are distributed over a line. This leads, nonetheless, to results consistent with the many trends observed in jet dynamics and sound radiation.

Each problem can be separately solved using the resolvent formalism, such that,

$$p = \mathcal{R}_{\text{Helmholtz}}[q], \quad (65)$$

and

$$q = \mathcal{R}_{\text{G-L}}[f]. \quad (66)$$

In matrix form, p and f can be directly related as,

$$p = \mathbf{R}_{\text{Helmholtz}} \mathbf{R}_{\text{G-L}} f, \quad (67)$$

and we thus define $\mathbf{R}_{\text{coupled}} = \mathbf{R}_{\text{Helmholtz}} \mathbf{R}_{\text{G-L}}$ as the resolvent operator of the coupled problem, going from forcing terms in the Ginzburg-Landau equation to an acoustic field. A singular-value decomposition of $\mathbf{R}_{\text{coupled}}$ shows optimal forcing for generation of an acoustic radiation measured in p .

5.2 Acoustic radiation due to a stochastic forcing term (example14.m)

The methods elaborated in section 2 can be applied to the coupled resolvent operator defined above. As an example, we use the Ginzburg-Landau system with the same parameters used in section 4.3 $A = 0.6$, $k_h = 1$, $\omega = 1$, and with

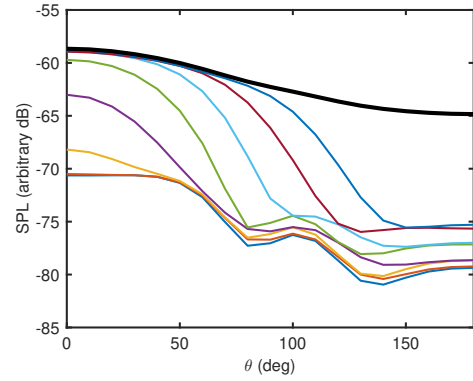


Fig. 28: Acoustic radiation of the coupled Ginzburg-Landau/acoustic problem. The thick black line shows the full sound radiation considering the model forcing P_{ff} from eq. (62). Lower lines show sound radiation with increasing number of SPOD modes of q considered in the acoustic problem (from 1 to 8 SPOD modes).

a short coherence length scale, $L_c = 0.1$. Our attention will be restricted to the subsonic case, $M = 0.6$, due the higher relevance of jitter for subsonic jet-noise.²⁰

With the above considerations, the radiated sound field is shown in figure 28 as a thick black line, indicating the SPL corresponding to the radiated power spectral density. Given the Gaussian wavepacket shape of q , resulting from the forced Ginzburg-Landau equation discussed in section 4, the calculated sound field has a directivity shape similar to what was given by the model sources in section 3.

The contributions of individual SPOD modes in the source wavepacket, q , to the radiated sound can now be evaluated. *Partial* reconstructions of P_{qq} , using a limited number of leading SPOD modes, can be used to obtain the acoustic field; these results are shown in figure 28 as thin coloured lines. We notice that there is a slow convergence to the full radiated sound, indicating that wavepacket jitter is relevant. The first SPOD mode of q leads to an underprediction of peak radiation of about 17dB, and a superposition of 5 SPOD modes of q is necessary to obtain a sound field close to that produce by the full source for low polar angles.

5.3 Resolvent modes of the coupled problem

Instead of using an SPOD of the “flow” variable, q , which serves as a source term in the inhomogeneous Helmholtz equation, one may take the SVD of the coupled resolvent operator, $\mathbf{R}_{\text{coupled}}$, to obtain the optimal relationship between forcing terms, f and the response in the radiated sound; the forcing CSD, P_{ff} , may then be projected onto the forcing modes to reconstruct the acoustic field. Such a reconstruction is shown in figure 29²¹. When compared to the acoustic radiation of SPOD modes of q shown in figure

²⁰Results were obtained using the script example14.m. The acoustic field is discretised from 0 to 180° in steps of 10°, with observers placed at $R = 200/k$, where k is the acoustic wavenumber.

²¹Figure also generated with script example14.m. Note that weight matrices need to be included in resolvent analysis, as in section 4.

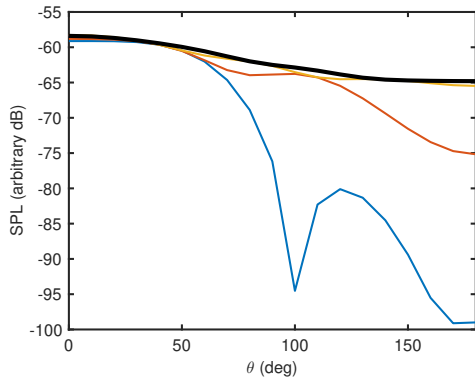


Fig. 29: Reconstruction of the radiated sound from a forcing CSD P_{ff} using resolvent modes of $\mathbf{R}_{\text{coupled}}$. The thick black line shows the full PSD of pressure, and remaining lines show reconstruction with 1, 2 or 3 resolvent modes.

28, the convergence to the full radiation in figure 29 is much faster: a single mode already gives an accurate low-angle radiation, and three modes recover virtually all of the radiated sound.

The resolvent modes of $\mathbf{R}_{\text{coupled}}$, shown in figure 30, highlight a different mechanism when acoustic radiation is taken as the relevant flow response. The first forcing mode of the coupled problem has a slight peak near the inflow at $x = 0$, but also includes distributed forcing through the domain, with a large wavelength, and thus a large phase speed. This leads to supersonic components in the flow mode, which has a basic wavepacket shape similar to the standard Ginzburg-Landau responses (compare with figure 24), but with changes in the amplitude envelope. The supersonic forcing function leads to supersonic components in the flow response, increasing the acoustic matching and leading to the beamed radiation seen in the acoustic response mode 1 of figure 29. This effect is even more pronounced for the second mode: here, the forcing has nearly constant real and imaginary parts, which is indicative of a near-infinite phase speed in x . This also leads to changes in the basic wavepacket shape of flow mode 2, which now has components with high phase speed that match the acoustic dispersion relation, leading to significant sound radiation. The infinite phase speed appearing in the flow mode due to the forcing matches the phase speed of acoustic waves radiated in the sideline direction, $\theta = 90^\circ$, and this is observed in the acoustic response mode 2.

These results, taken from a model problem, are similar to what Jeun *et al.* [49] found in their resolvent analysis of a Mach 0.9 jet, using the acoustic radiation as the output. The first two forcing and response modes for $St=0.56$, taken from that work, are shown in figure 31. We note that, unlike resolvent analysis that considers flow fluctuations as the output (as done by Schmidt *et al.* [38] and Lesshafft *et al.* [51]), which lead to optimal forcing modes near the nozzle exit or inside the pipe, the forcing modes seen in figure 31 are spatially extended. For $St = 0.56$ and $M = 0.9$, the acoustic wavelength is equal to 2 jet diameters, or 4 radii; the wavelengths

in figure 31 are of about 6 jet radii, and we thus have forcings with supersonic speeds, similar to what we observed for the forcing modes in the coupled Ginzburg-Landau/acoustic problem shown in figure 30. The optimal response shows superdirective radiation towards the downstream direction, while the first suboptimal has a double-beam structure.

A final remark concerns supersonic jets. As would be expected from the discussion in section 3, a supersonic wavepacket has Mach-wave radiation, and the standard amplification mechanism of the Ginzburg-Landau equation, explored in section 4, leads to a wavepacket with supersonic phase speed radiating directly to the acoustic field, with a comparably minor role of jitter. Upstream forcing near $x = 0$ is thus efficient for the generation of acoustic radiation if the Mach number is supersonic, and the resolvent modes of the coupled problem (with $\mathbf{R}_{\text{coupled}}$) are very similar to the standard Ginzburg-Landau response modes; they are not shown here, but can be easily obtained using the provided scripts. The dominance of the leading resolvent mode in the Ginzburg-Landau system, associated with the convective amplification, translates thus directly to the acoustic field when the coupled problem is considered. This is shown in figure 32. Subsonic Mach numbers have relatively flat leading gains, with no clear dominance of the optimal forcing/response pair; we have illustrated the mechanisms in figure 30. However, when the Mach number is increased to the supersonic range, the first gain becomes significantly higher than the suboptimals, and the first mode is related to Mach-wave radiation. Figure 32 is quite similar to the corresponding result for jets in Jeun *et al.* [49], reproduced in fig. 32(b).

6 Conclusion and outlook

We have considered coherent structures in turbulent jets, with respect both to their dynamic underpinnings and the mechanisms by which they generate sound. Both are discussed in a framework provided by the resolvent of the linearised Navier-Stokes equations, this being found to provide a unifying fabric that connects aeroacoustic and linear-stability theories. This is discussed in section 2, where the problems are considered in input-output form, the input being either an acoustic-analogy source term or the non-linear terms from the governing equations, and the output, accordingly, either farfield sound-pressure fluctuations or hydrodynamic near-field flow fluctuations.

Our treatment of the problem involves consideration of two simplified models. In Section 3 the inhomogeneous Helmholtz equation that results from Lighthill's acoustic analogy is used to explore *kinematic* sound-source models that mimic wavepacket activity observed in turbulent jets. While in section 4, simplified *dynamic* models are considered, these being based on the inhomogeneous, linearised Ginzburg-Landau equation, that we use as a surrogate for the inhomogeneous, linearised Navier-Stokes system. A coupled system, where the output from the dynamic, Ginzburg-Landau model is used as an input for the kinematic, acoustic-analogy model, is presented in section 5, illustrating a simplified setting that involves both wavepacket dynamics and

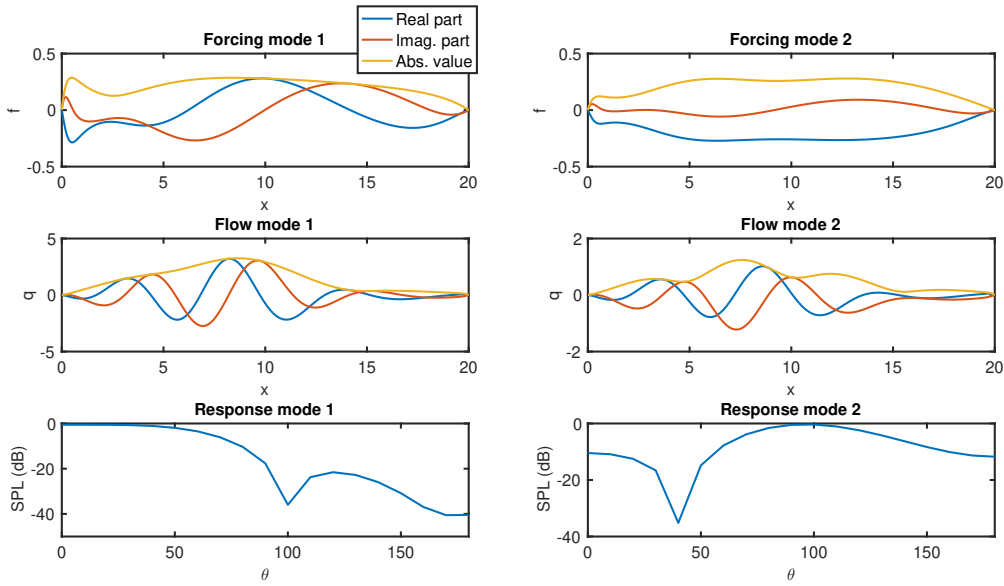


Fig. 30: Resolvent modes of $\mathbf{R}_{\text{coupled}}$

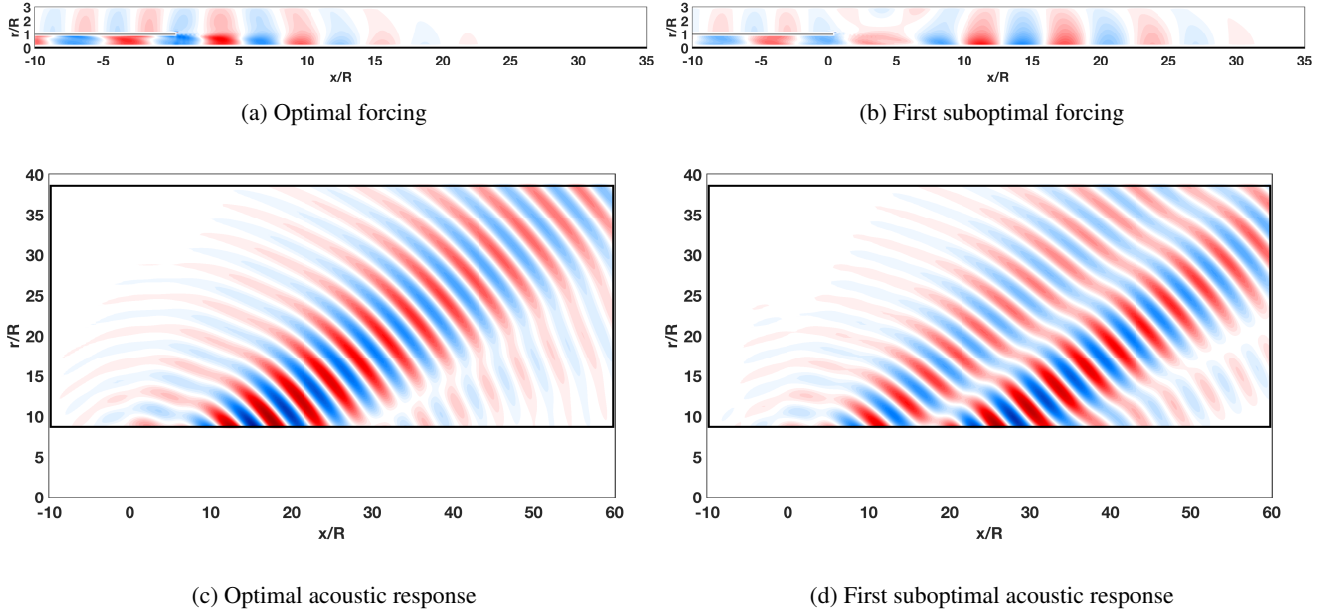
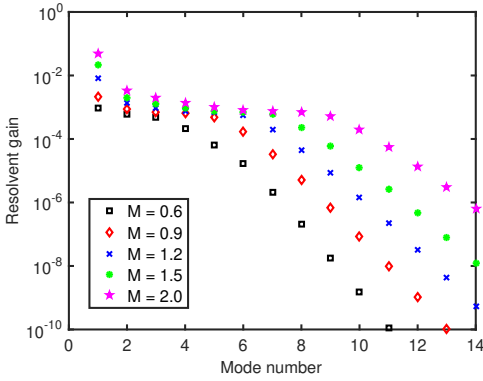


Fig. 31: Optimal and first suboptimal x -momentum forcing modes and corresponding responses for a Mach 0.9 jet at $St=0.56$, considering acoustic pressure as the output. Grey lines in subfigures (a) and (b) mark the nozzle, and rectangles in subfigures (c) and (d) highlight the domain considered for the acoustic response. Results from Jeun *et al.* [49].

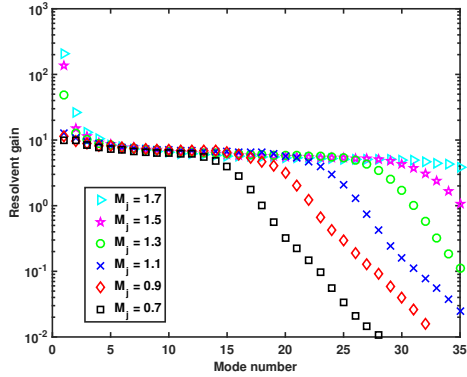
sound radiation. Despite the simplicity of the models, they are found to reproduce many relevant features observed in experiments and simulations of turbulent jets. The models are accompanied by Matlab/Octave scripts in the supplementary material, and we propose the ensemble as a platform for the development of understanding both of the modelling approaches discussed and the flow physics they mimic.

We close this review with a discussion on the practical relevance of wavepacket models, especially given that current large-eddy simulations allow accurate predictions of

sound radiation of turbulent jets, with errors of less than 1dB, with relatively low computational cost [7, 110]; in such a scenario, one may question the need or the relevance of simplified, reduced-order models when an accurate simulation can be carried out. In our view, linear wavepacket modelling frameworks reviewed here can be useful in diverse ways. They provide a basis for the estimation of sound radiation with reduced computational cost (in comparison to high-fidelity simulations). Examples include the use of kinematic wave-packet sound-source models by Neilsen *et al.* [111],



(a) Coupled Ginzburg-Landau acoustic problem



(b) Turbulent jet

Fig. 32: Leading resolvent gains for various Mach numbers. Gains for the turbulent jet taken from Jeun *et al.* [49].

who use ground acoustic measurements of military aircraft to calibrate source models that are then used to obtain far-field radiation; or the work of Papamoschou [85], who uses self-similar kinematic wave-packet models, calibrated with measured spectra, to obtain sound radiation at other positions. Dynamic modelling approaches, such as that of Towne *et al.* [67], on the other hand, aim to determine models for the statistics of non-linear forcing terms from high-fidelity simulation data, and that would allow the dynamics of coherent structures and sound to be obtained from the linearised Navier-Stokes equations using the resolvent framework.

The frameworks also provide a basis for analysis and understanding of the mechanisms that underpin both the dynamics of coherent structures in jets and the sound these radiate; as such they constitute a foundation on which to develop jet-noise reduction methodologies. Devices for open-loop control, such as tabs and chevrons [112] or microjets [113], are known to reduce the sound radiated by subsonic and supersonic jets, but they are often developed on a trial-and-error basis in laboratory experiments, and their effectiveness in flight conditions has been questioned [114]. The development of such technologies would benefit from the more solid theoretical footing that is provided by the dynamic modelling framework discussed. Indeed, dynamic wavepacket models have been successfully used to understand noise-control re-

sults [115, 116, 117, 118], and may serve in the design of low-noise nozzles. Examples of how they may guide improvement in microjet design can be found in the work of Le Rallic *et al.* [119] and Sinha *et al.* [120]. Their use for the elaboration of closed-loop control strategies is also a promising future direction. Wavepacket models have already been used for the estimation of turbulent-jet fluctuations from limited numbers of sensors [121, 122], and this is the basis for the definition of control laws, actuation being driven by sensor measurements so as to cancel incoming wavepackets. A proof of concept of wave cancellation for harmonically excited turbulent jets has been provided by Kopiev *et al.* [123], and a closed-loop control study was successfully implemented by Sasaki *et al.* for the simpler case of a low Reynolds number mixing layer [124]. The foregoing approaches for both open- and closed-loop control of jet noise have been reviewed by Cavalieri [125].

Perhaps the most important outcome, however, is the provision of deeper understanding of the flow physics that underpin coherent structures in jets and the sound they produce. The analysis of non-linear systems is a difficult task, and, while progress may be made using methods from non-linear dynamical-systems theory [126], simplification of the problem as a linear system with stochastic forcing, reviewed in section 2, has led to substantial progress in the study of jet turbulence and sound radiation, and is likely to open new research directions. Some recent examples exist in which these simplified linear modelling frameworks have led both to new insight, and to the anticipation or prediction of how a complex system will behave subject to a given modification. The kinematic [127, 79] and dynamic [128, 129] modelling approaches have, for instance, provided substantial clarification of the sound-source mechanisms associated with installed jet-noise, i.e. sound radiation of jets in the vicinity of wings. The studies show how the near pressure field of jet wavepackets is scattered by the wing trailing edge, leading to significant increases in sound radiation. The results were based on the use of a tailored Green's function that accounts for the presence of the neighbouring surface and may be dealt with using the formalisms outlined in sections 2 and 3, either by replacing the free-space Green's function with its tailored counterpart, or by incorporating the wing trailing edge as a boundary condition for the linear operator of the dynamic model. The results of the studies allowed an anticipation of a beneficial effect that would be produced by inclining the trailing edge relative to the jet, and this was confirmed both by models and experiment in the work of Piantanida *et al.* [130].

Another example is the detection of trapped acoustic waves (informally known as “punk modes”) in the potential core of high-subsonic jets. This phenomenon could be thoroughly modelled using simplified linearised models, albeit with an approach different to that described in section 4: the main mechanisms can be described by simplifying the jet as a compressible vortex sheet, or even further by considering it to behave as a soft acoustic duct with uniform flow [131]. The simplified linear models led to a rather complete explanation of the physics involved both in the more

complete global analysis [105], the high-fidelity simulation and the experiments [7]. Understanding of the fundamental physics of these trapped waves provided by the simplified models led, again, to a rather complete explanation, by Jordan *et al.* [132], of the flow physics involved in the generation of high-amplitude tones that result when a turbulent jet grazes a sharp edge [133], such as the trailing edge of a wing. Similar analyses for supersonic jets have provided more complete understanding of tonal dynamics associated with impinging [134, 135] and screeching jets [136, 137].

We close our discussion with an emphasis of the fact that, while simplified descriptions of the complex flow behaviour involved in jet noise are essential, there remains a need for accurate, detailed experiments and carefully validated numerical simulation of jet noise. The validity of simplified models can only be determined by comparison with high-fidelity data from experiments or simulations, and such data require dedicated post-processing to extract quantities directly comparable to wavepacket-model predictions. These comparative studies require considerable organisation and forward planning in order to ensure that perspicacious use be made of the enormous datasets produced by experiment and simulation. Such was the case for the recent experiment by Jaunet *et al.* [17] and the simulation and experiment by Brès *et al.* [7], both of which now serve as a basis for new development of wavepacket models. The relevance of wavepacket jitter for sound radiation, that we have reviewed, poses a challenge in terms of data analysis, as the convergence of two-point statistics, with accuracy sufficient for modelling purposes, is slow and requires huge quantities of data, as illustrated by applications using simulation [138] and experimental data [51]: increasing the number of samples leads to a slow convergence of higher-order SPOD modes, which, while secondary in terms of their energetic content, are crucial for the description of wavepacket jitter and sound radiation. Collaborative efforts in the research community, with strong interaction between theory, simulation and experiment, are the key to progress in future jet-noise research.

Acknowledgements

This review sums up ideas developed in a long-term collaborative effort — the *wavepacketfest* — involving a large number of colleagues. We would like to thank in particular Anurag Agarwal, P. Apu, Guillaume Brès, Tim Colonius, Eduardo Martini, Petrônio Nogueira, Daniel Rodríguez, Kenzo Sasaki, Oliver Schmidt, Léopold Shaabani Ardali, Gilles Tissot and Aaron Towne for the discussions related to the work reviewed here. We would also like to thank David Breakey, Guillaume Brès, Oguzhan Kaplan, Jinah Jeun, Igor Maia, Joseph Nichols and Aniruddha Sinha for kindly sharing data or preparing some of the figures in this work. Some of the present material evolved from a course given by the first author in the FLOW School “Aeroacoustics & Thermoacoustics of Propulsion Systems”, on October 2017; Mihai Mihaescu, Philipp Schlatter, Ardeshir Hanifi and Dan Henningson are warmly acknowledged.

References

- [1] Cavalieri, A. V. G., Rodríguez, D., Jordan, P., Colonius, T., and Gervais, Y., 2013. “Wavepackets in the velocity field of turbulent jets”. *Journal of Fluid Mechanics*, **730**, 9, pp. 559–592.
- [2] Fuchs, H. V., and Michel, U., 1978. “Experimental evidence of turbulent source coherence affecting jet noise”. *AIAA Journal*, **16**(9), pp. 871–872.
- [3] Juvé, D., Sunyach, M., and Comte-Bellot, G., 1979. “Filtered azimuthal correlations in the acoustic far field of a subsonic jet”. *AIAA Journal*, **17**, p. 112.
- [4] Kopiev, V., Zaitsev, M., Velichko, S., Kotova, A., and Belyaev, I., 2008. “Cross-correlations of far field azimuthal modes in subsonic jet noise”. In 14th AIAA/CEAS Aeroacoustics Conference (29th AIAA Aeroacoustics Conference), p. 2887.
- [5] Cavalieri, A. V. G., Jordan, P., Colonius, T., and Gervais, Y., 2012. “Axisymmetric superdirectivity in subsonic jets”. *Journal of Fluid Mechanics*, **704**, p. 388.
- [6] Faranosov, G. A., Belyaev, I. V., Kopiev, V. F., Zaytsev, M. Y., Aleksentsev, A. A., Bersenev, Y. V., Chursin, V. A., and Viskova, T. A., 2016. “Adaptation of the azimuthal decomposition technique to jet noise measurements in full-scale tests”. *AIAA Journal*, **55**(2), pp. 572–584.
- [7] Brès, G. A., Jordan, P., Jaunet, V., Le Rallic, M., Cavalieri, A. V., Towne, A., Lele, S. K., Colonius, T., and Schmidt, O. T., 2018. “Importance of the nozzle-exit boundary-layer state in subsonic turbulent jets”. *Journal of Fluid Mechanics*, **851**, pp. 83–124.
- [8] Brès, G. A., Ham, F. E., Nichols, J. W., and Lele, S. K., 2017. “Unstructured large-eddy simulations of supersonic jets”. *AIAA Journal*, pp. 1164–1184.
- [9] Mollo-Christensen, E., 1967. “Jet noise and shear flow instability seen from an experimenter’s viewpoint (Similarity laws for jet noise and shear flow instability as suggested by experiments)”. *Journal of Applied Mechanics*, **34**, pp. 1–7.
- [10] Lau, J. C., Fisher, M. J., and Fuchs, H. V., 1972. “The intrinsic structure of turbulent jets”. *Journal of Sound and Vibration*, **22**(4), pp. 379–384.
- [11] Michalke, A., and Fuchs, H. V., 1975. “On turbulence and noise of an axisymmetric shear flow”. *Journal of Fluid Mechanics*, **70**, pp. 179–205.
- [12] Armstrong, R. R., Fuchs, H. V., and Michalke, A., 1977. “Coherent structures in jet turbulence and noise”. *AIAA Journal*, **15**, pp. 1011–1017.
- [13] Tinney, C. E., and Jordan, P., 2008. “The near pressure field of co-axial subsonic jets”. *Journal of Fluid Mechanics*, **611**, pp. 175–204.
- [14] Breakey, D. E., Jordan, P., Cavalieri, A. V., Nogueira, P. A., Léon, O., Colonius, T., and Rodríguez, D., 2017. “Experimental study of turbulent-jet wave packets and their acoustic efficiency”. *Physical Review Fluids*, **2**(12), p. 124601.
- [15] Jung, D., Gamard, S., and George, W. K., 2004. “Downstream evolution of the most energetic modes in a turbulent axisymmetric jet at high Reynolds num-

- ber. Part 1. The near-field region”. *Journal of Fluid Mechanics*, **514**, pp. 173–204.
- [16] Suzuki, T., and Colonius, T., 2006. “Instability waves in a subsonic round jet detected using a near-field phased microphone array”. *Journal of Fluid Mechanics*, **565**, pp. 197–226.
- [17] Jaunet, V., Jordan, P., and Cavalieri, A., 2017. “Two-point coherence of wave packets in turbulent jets”. *Physical Review Fluids*, **2**(2), p. 024604.
- [18] Crow, S. C., and Champagne, F. H., 1971. “Orderly structure in jet turbulence”. *Journal of Fluid Mechanics*, **48**(3), pp. 547–591.
- [19] Moore, C. J., 1977. “The role of shear-layer instability waves in jet exhaust noise”. *Journal of Fluid Mechanics*, **80**(2), pp. 321–367.
- [20] Michalke, A., 1971. “Instabilität eines Kompressiblen Runden Freistrahls unter Berücksichtigung des Einflusses der Strahlgrenzschichtdicke”. *Zeitschrift für Flugwissenschaften*, **19**, pp. 319–328; English translation: NASA TM 75190, 1977.
- [21] Crighton, D. G., and Gaster, M., 1976. “Stability of slowly diverging jet flow”. *Journal of Fluid Mechanics*, **77**(2), pp. 397–413.
- [22] Sasaki, K., Cavalieri, A. V., Jordan, P., Schmidt, O. T., Colonius, T., and Brès, G. A., 2017. “High-frequency wavepackets in turbulent jets”. *Journal of Fluid Mechanics*, **830**.
- [23] Schmid, P. J., and Henningson, D. S., 2001. *Stability and transition in shear flows*, Vol. 142. Springer.
- [24] Criminale, W. O., Jackson, T. L., and Joslin, R. D., 2003. *Theory and computation of hydrodynamic stability*. Cambridge Univ Pr.
- [25] Schmid, P. J., 2007. “Nonmodal stability theory”. *Annual Review of Fluid Mechanics*, **39**, pp. 129–162.
- [26] Juniper, M. P., Hanifi, A., and Theofilis, V., 2014. “Modal stability theory — lecture notes from the flow-nordita summer school on advanced instability methods for complex flows, stockholm, sweden, 2013”. *Applied Mechanics Reviews*, **66**(2), p. 024804.
- [27] Schmid, P. J., and Brandt, L., 2014. “Analysis of fluid systems: Stability, receptivity, sensitivity”. *Applied Mechanics Reviews*, **66**(2), p. 024803.
- [28] Kim, J., and Bewley, T. R., 2007. “A linear systems approach to flow control”. *Annu. Rev. Fluid Mech.*, **39**, pp. 383–417.
- [29] Bagheri, S., Henningson, D., Hoepffner, J., and Schmid, P., 2009. “Input-output analysis and control design applied to a linear model of spatially developing flows”. *Applied Mechanics Reviews*, **62**(2), p. 020803.
- [30] Fabbiane, N., Semeraro, O., Bagheri, S., and Henningson, D. S., 2014. “Adaptive and model-based control theory applied to convectively unstable flows”. *Applied Mechanics Reviews*, **66**(6), p. 060801.
- [31] Sipp, D., and Schmid, P. J., 2016. “Linear closed-loop control of fluid instabilities and noise-induced perturbations: A review of approaches and tools”. *Applied Mechanics Reviews*, **68**(2), p. 020801.
- [32] Farrell, B. F., and Ioannou, P. J., 1993. “Stochastic forcing of the linearized navier–stokes equations”. *Physics of Fluids A: Fluid Dynamics*, **5**(11), pp. 2600–2609.
- [33] Jovanović, M. R., and Bamieh, B., 2005. “Componentwise energy amplification in channel flows”. *Journal of Fluid Mechanics*, **534**, pp. 145–183.
- [34] McKeon, B., and Sharma, A., 2010. “A critical-layer framework for turbulent pipe flow”. *Journal of Fluid Mechanics*, **658**, pp. 336–382.
- [35] Hwang, Y., and Cossu, C., 2010. “Linear non-normal energy amplification of harmonic and stochastic forcing in the turbulent channel flow”. *Journal of Fluid Mechanics*, **664**, pp. 51–73.
- [36] Semeraro, O., Jaunet, V., Jordan, P., Cavalieri, A. V., and Lesshafft, L., 2016. “Stochastic and harmonic optimal forcing in subsonic jets”. In 22nd AIAA/CEAS Aeroacoustics Conference, p. 2935.
- [37] Towne, A., Schmidt, O. T., and Colonius, T., 2018. “Spectral proper orthogonal decomposition and its relationship to dynamic mode decomposition and resolvent analysis”. *Journal of Fluid Mechanics*, **847**, pp. 821–867.
- [38] Schmidt, O. T., Towne, A., Rigas, G., Colonius, T., and Brès, G. A., 2018. “Spectral analysis of jet turbulence”. *Journal of Fluid Mechanics*, **855**, pp. 953–982.
- [39] Garnaud, X., Lesshafft, L., Schmid, P., and Huerre, P., 2013. “The preferred mode of incompressible jets: linear frequency response analysis”. *Journal of Fluid Mechanics*, **716**, pp. 189–202.
- [40] Jordan, P., and Colonius, T., 2013. “Wave packets and turbulent jet noise”. *Annual Review of Fluid Mechanics*, **45**(1).
- [41] Waleffe, F., 1997. “On a self-sustaining process in shear flows”. *Physics of Fluids*, **9**(4), pp. 883–900.
- [42] Moehlis, J., Faisst, H., and Eckhardt, B., 2004. “A low-dimensional model for turbulent shear flows”. *New Journal of Physics*, **6**(1), p. 56.
- [43] Barkley, D., 2016. “Theoretical perspective on the route to turbulence in a pipe”. *Journal of Fluid Mechanics*, **803**.
- [44] Lighthill, M. J., 1952. “On sound generated aerodynamically. I. General theory”. *Proceedings of the Royal Society of London. Series A, Mathematical and Physical Sciences*, pp. 564–587.
- [45] Crighton, D. G., 1975. “Basic principles of aerodynamic noise generation”. *Progress in Aerospace Sciences*, **16**(1), pp. 31–96.
- [46] Goldstein, M. E., 2003. “A generalized acoustic analogy”. *Journal of Fluid Mechanics*, **488**, pp. 315–333.
- [47] McKeon, B., 2017. “The engine behind (wall) turbulence: perspectives on scale interactions”. *Journal of Fluid Mechanics*, **817**.
- [48] Garnaud, X., Sandberg, R. D., and Lesshafft, L., 2013. “Global response to forcing in a subsonic jet: instability wavepackets and acoustic radiation”. In 19th AIAA/CEAS Aeroacoustics Conference, p. 2232.

- [49] Jeun, J., Nichols, J. W., and Jovanović, M. R., 2016. “Input-output analysis of high-speed axisymmetric isothermal jet noise”. *Physics of Fluids*, **28**(4), p. 047101.
- [50] Tissot, G., Zhang, M., Lajús, F. C., Cavalieri, A. V., and Jordan, P., 2017. “Sensitivity of wavepackets in jets to nonlinear effects: the role of the critical layer”. *Journal of Fluid Mechanics*, **811**, pp. 95–137.
- [51] Lesshafft, L., Semeraro, O., Jaunet, V., Cavalieri, A. V. G., and Jordan, P., 2018. “Resolvent-based modelling of coherent wavepackets in a turbulent jet”. *arXiv preprint arXiv:1810.09340*.
- [52] Huerre, P., and Monkewitz, P. A., 1990. “Local and global instabilities in spatially developing flows”. *Annual Review of Fluid Mechanics*, **22**(1), pp. 473–537.
- [53] Monkewitz, P. A., Huerre, P., and Chomaz, J.-M., 1993. “Global linear stability analysis of weakly non-parallel shear flows”. *Journal of Fluid Mechanics*, **251**, pp. 1–20.
- [54] Goldstein, M. E., and Leib, S. J., 2005. “The role of instability waves in predicting jet noise”. *Journal of Fluid Mechanics*, **525**, pp. 37–72.
- [55] Cohen, J., and Wygnanski, I., 1987. “The evolution of instabilities in the axisymmetric jet. part 1. the linear growth of disturbances near the nozzle”. *Journal of Fluid Mechanics*, **176**, pp. 191–219.
- [56] Bendat, J., and Piersol, A., 1986. *Random data: analysis and measurement procedures*. Wiley-Interscience.
- [57] Berkooz, G., Holmes, P., and Lumley, J., 1993. “The proper orthogonal decomposition in the analysis of turbulent flows”. *Annual Review of Fluid Mechanics*, **25**(1), pp. 539–575.
- [58] Rowley, C. W., and Dawson, S. T., 2017. “Model reduction for flow analysis and control”. *Annual Review of Fluid Mechanics*, **49**, pp. 387–417.
- [59] Taira, K., Brunton, S. L., Dawson, S. T., Rowley, C. W., Colonius, T., McKeon, B. J., Schmidt, O. T., Gordeyev, S., Theofilis, V., and Ukeiley, L. S., 2017. “Modal analysis of fluid flows: An overview”. *Aiaa Journal*, pp. 4013–4041.
- [60] Picard, C., and Delville, J., 2000. “Pressure velocity coupling in a subsonic round jet”. *International Journal of Heat and Fluid Flow*, **21**(3), pp. 359–364.
- [61] Chomaz, J. M., 2005. “Global instabilities in spatially developing flows: non-normality and nonlinearity”. *Annual Review of Fluid Mechanics*, **37**, pp. 357–392.
- [62] Farrell, B. F., and Ioannou, P. J., 2014. “Statistical state dynamics: a new perspective on turbulence in shear flow”. *arXiv preprint arXiv:1412.8290*.
- [63] Beneddine, S., Sipp, D., Arnault, A., Dandois, J., and Lesshafft, L., 2016. “Conditions for validity of mean flow stability analysis”. *Journal of Fluid Mechanics*, **798**, pp. 485–504.
- [64] Wu, X., and Huerre, P., 2009. “Low-frequency sound radiated by a nonlinearly modulated wavepacket of helical modes on a subsonic circular jet”. *Journal of Fluid Mechanics*, **637**, pp. 173–211.
- [65] Suponitsky, V., Sandham, N., and Morfey, C., 2010. “Linear and nonlinear mechanisms of sound radiation by instability waves in subsonic jets”. *Journal of Fluid Mechanics*, **658**, pp. 509–538.
- [66] Suponitsky, V., Sandham, N., and Agarwal, A., 2011. “On the Mach number and temperature dependence of jet noise: Results from a simplified numerical model”. *Journal of Sound and Vibration*.
- [67] Towne, A., Bres, G. A., and Lele, S. K., 2017. “A statistical jet-noise model based on the resolvent framework”. In 23rd AIAA/CEAS Aeroacoustics Conference, p. 3706.
- [68] Mollo-Christensen, E., 1963. Measurements of near field pressure of subsonic jets. Tech. rep., Advisory Group for Aeronautical Research and Development, Paris, France.
- [69] Mollo-Christensen, E., Kolpin, M. A., and Martuccelli, J. R., 1964. “Experiments on jet flows and jet noise far-field spectra and directivity patterns”. *Journal of Fluid Mechanics*, **18**(2), pp. 285–301.
- [70] Crow, S. C., 1972. “Acoustic gain of a turbulent jet”. In Phys. Soc. Meeting, Univ. Colorado, Boulder, paper IE, Vol. 6.
- [71] Ffowcs Williams, J. E., and Kempton, A. J., 1978. “The noise from the large-scale structure of a jet”. *Journal of Fluid Mechanics*, **84**(4), pp. 673–694.
- [72] Crighton, D. G., and Huerre, P., 1990. “Shear-layer pressure fluctuations and superdirective acoustic sources”. *Journal of Fluid Mechanics*, **220**, pp. 355–368.
- [73] Cavalieri, A. V. G., Jordan, P., Agarwal, A., and Gervais, Y., 2011. “Jittering wave-packet models for subsonic jet noise”. *Journal of Sound and Vibration*, **330**(18-19), pp. 4474–4492.
- [74] Cavalieri, A. V. G., and Agarwal, A., 2014. “Coherence decay and its impact on sound radiation by wavepackets”. *Journal of Fluid Mechanics*, **748**, pp. 399–415.
- [75] Ffowcs Williams, J. E., 1963. “The noise from turbulence convected at high speed”. *Philosophical Transactions of the Royal Society of London. Series A, Mathematical and Physical Sciences*, **255**(1061), pp. 469–503.
- [76] Freund, J. B., 2001. “Noise sources in a low-Reynolds-number turbulent jet at Mach 0.9”. *Journal of Fluid Mechanics*, **438**, pp. 277–305.
- [77] Cabana, M., Fortuné, V., and Jordan, P., 2008. “Identifying the radiating core of Lighthill’s source term”. *Theoretical and Computational Fluid Dynamics*, **22**(2), pp. 87–106.
- [78] Baqui, Y. B., Agarwal, A., Cavalieri, A. V., and Sinayoko, S., 2015. “A coherence-matched linear source mechanism for subsonic jet noise”. *Journal of Fluid Mechanics*, **776**, pp. 235–267.
- [79] Nogueira, P. A., Cavalieri, A. V., and Jordan, P., 2017. “A model problem for sound radiation by an installed jet”. *Journal of Sound and Vibration*, **391**, pp. 95–115.
- [80] Kopiev, V., Chernyshev, S., Faranosov, G., Zaitsev,

- M., and Belyaev, I., 2010. "Correlations of jet noise azimuthal components and their role in source identification". In 16th AIAA/CEAS Aeroacoustics Conference and Exhibit.
- [81] Reba, R., Narayanan, S., and Colonius, T., 2010. "Wave-packet models for large-scale mixing noise". *International Journal of Aeroacoustics*, **9**(4), pp. 533–558.
- [82] Suzuki, T., 2013. "Coherent noise sources of a subsonic round jet investigated using hydrodynamic and acoustic phased-microphone arrays". *Journal of Fluid Mechanics*, **730**, pp. 659–698.
- [83] Freund, J. B., 2003. "Noise-source turbulence statistics and the noise from a mach 0.9 jet". *Physics of Fluids*, **15**(6), pp. 1788–1799.
- [84] Morris, P. J., 2009. "A note on noise generation by large scale turbulent structures in subsonic and supersonic jets". *International Journal of Aeroacoustics*, **8**(4), pp. 301–315.
- [85] Papamoschou, D., 2018. "Wavepacket modeling of the jet noise source". *International Journal of Aeroacoustics*, **17**(1-2), pp. 52–69.
- [86] McLaughlin, D. K., Morrison, G. L., and Troutt, T. R., 1975. "Experiments on the instability waves in a supersonic jet and their acoustic radiation". *Journal of Fluid Mechanics*, **69**(1), pp. 73–95.
- [87] Papamoschou, D., 1997. "Mach wave elimination in supersonic jets". *AIAA journal*, **35**(10), pp. 1604–1611.
- [88] Tam, C. K., Chen, P., and Seiner, J., 1992. "Relationship between the instability waves and noise of high-speed jets". *AIAA journal*, **30**(7), pp. 1747–1752.
- [89] Tam, C. K., 1995. "Supersonic jet noise". *Annual Review of Fluid Mechanics*, **27**(1), pp. 17–43.
- [90] Laufer, J., and Yen, T.-C., 1983. "Noise generation by a low-Mach-number jet". *Journal of Fluid Mechanics*, **134**, pp. 1–31.
- [91] Sinha, A., Rodríguez, D., Brès, G. A., and Colonius, T., 2014. "Wavepacket models for supersonic jet noise". *Journal of Fluid Mechanics*, **742**, pp. 71–95.
- [92] Lighthill, M. J., 1954. "On sound generated aerodynamically. II. Turbulence as a source of sound". *Proceedings of the Royal Society of London. Series A. Mathematical and Physical Sciences*, **222**(1148), p. 1.
- [93] Freund, J. B., and Colonius, T., 2009. "Turbulence and sound-field POD analysis of a turbulent jet". *International Journal of Aeroacoustics*, **8**(4), pp. 337–354.
- [94] Towne, A., Colonius, T., Jordan, P., Cavalieri, A. V. G., and Brès, G. A., 2015. "Stochastic and nonlinear forcing of wavepackets in a mach 0.9 jet". In 21st AIAA/CEAS Aeroacoustics Conference, p. 2217.
- [95] Huerre, P., 2000. "Open shear flow instabilities". In *Perspectives in Fluid Dynamics*, G. Batchelor, H. Moffatt, and M. Worster, eds. Cambridge University Press, pp. 159–229.
- [96] Lesshafft, L., and Huerre, P., 2007. "Linear impulse response in hot round jets". *Physics of Fluids (1994-present)*, **19**(2), p. 024102.
- [97] Rodríguez, D., Cavalieri, A. V., Colonius, T., and Jordan, P., 2015. "A study of linear wavepacket models for subsonic turbulent jets using local eigenmode decomposition of piv data". *European Journal of Mechanics-B/Fluids*, **49**, pp. 308–321.
- [98] Monkewitz, P. A., and Sohn, K. D., 1988. "Absolute instability in hot jets". *AIAA journal*, **26**, pp. 911–916.
- [99] Chomaz, J., Huerre, P., and Redekopp, L., 1988. "Bifurcations to local and global modes in spatially developing flows". *Physical Review Letters*, **60**(1), p. 25.
- [100] Weideman, J. A., and Reddy, S. C., 2000. "A matlab differentiation matrix suite". *ACM Transactions on Mathematical Software (TOMS)*, **26**(4), pp. 465–519.
- [101] Lesshafft, L., 2018. "Artificial eigenmodes in truncated flow domains". *Theoretical and Computational Fluid Dynamics*, **32**(3), pp. 245–262.
- [102] Barkley, D., 2006. "Linear analysis of the cylinder wake mean flow". *EPL (Europhysics Letters)*, **75**(5), p. 750.
- [103] Coenen, W., Lesshafft, L., Garnaud, X., and Sevilla, A., 2017. "Global instability of low-density jets". *Journal of Fluid Mechanics*, **820**, pp. 187–207.
- [104] Chakravarthy, R., Lesshafft, L., and Huerre, P., 2018. "Global stability of buoyant jets and plumes". *Journal of Fluid Mechanics*, **835**, pp. 654–673.
- [105] Schmidt, O. T., Towne, A., Colonius, T., Cavalieri, A. V., Jordan, P., and Brès, G. A., 2017. "Wavepackets and trapped acoustic modes in a turbulent jet: coherent structure eduction and global stability". *Journal of Fluid Mechanics*, **825**, pp. 1153–1181.
- [106] Trefethen, L. N., 2000. *Spectral methods in MATLAB*, Vol. 10. Society for Industrial Mathematics.
- [107] Tissot, G., Lajús Jr, F. C., Cavalieri, A. V., and Jordan, P., 2017. "Wave packets and Orr mechanism in turbulent jets". *Physical Review Fluids*, **2**(9), p. 093901.
- [108] Colonius, T., and Lele, S. K., 2004. "Computational aeroacoustics: progress on nonlinear problems of sound generation". *Progress in Aerospace Sciences*, **40**(6), pp. 345–416.
- [109] Wang, M., Freund, J. B., and Lele, S. K., 2006. "Computational Prediction of Flow-Generated Sound". *Annual Review of Fluid Mechanics*, **38**, pp. 483–512.
- [110] Freund, J. B., 2019. "Nozzles, turbulence, and jet noise prediction". *Journal of Fluid Mechanics*, **860**, pp. 1–4.
- [111] Neilsen, T. B., Gee, K. L., Harker, B. M., and James, M. M., 2016. "Level-educed wavepacket representation of noise radiation from a high-performance military aircraft". In 54th AIAA Aerospace Sciences Meeting, p. 1880.
- [112] Zaman, K., Bridges, J., and Huff, D., 2011. "Evolution from 'tabs' to 'chevron technology'-a review". *International Journal of Aeroacoustics*, **10**(5-6), pp. 685–709.
- [113] Henderson, B., 2010. "Fifty years of fluidic injection for jet noise reduction". *International Journal of Aeroacoustics*, **9**(1-2), pp. 91–122.
- [114] Shur, M. L., Spalart, P. R., and Strelets, M. K., 2011.

- “Les-based evaluation of a microjet noise reduction concept in static and flight conditions”. *Journal of Sound and Vibration*, **330**(17), pp. 4083–4097.
- [115] Kopiev, V., and Ostrikov, N., 2012. “Axisymmetrical instability wave control due to resonance coupling of azimuthal modes in high-speed jet issuing from corrugated nozzle”. In 18th AIAA/CEAS Aeroacoustics Conference (33rd AIAA Aeroacoustics Conference), p. 2144.
- [116] Lajús, F. C., Cavalieri, A. V., and Deschamps, C. J., 2015. “Spatial stability characteristics of non-circular jets”. In 21st AIAA/CEAS Aeroacoustics Conference, p. 2537.
- [117] Sinha, A., Xia, H., and Colonius, T., 2016. “Parabolized stability analysis of jets issuing from serrated nozzles”. *Fluid-Structure-Sound Interactions and Control*, p. 211.
- [118] Koenig, M., Sasaki, K., Cavalieri, A. V. G., Jordan, P., and Gervais, Y., 2016. “Jet-noise control by fluidic injection from a rotating plug: linear and non-linear sound-source mechanisms”. *Journal of Fluid Mechanics*, **788**, pp. 358–380.
- [119] Le Rallic, M., Jordan, P., and Gervais, Y., 2016. “Jet-noise reduction: the effect of azimuthal actuation modes”. In 22nd AIAA/CEAS Aeroacoustics Conference, p. 2868.
- [120] Sinha, A., Towne, A., Colonius, T., Schlinker, R. H., Reba, R., Simonich, J. C., and Shannon, D. W., 2017. “Active control of noise from hot supersonic jets”. *AIAA Journal*, **56**(3), pp. 933–948.
- [121] Sasaki, K., Piantanida, S., Cavalieri, A. V., and Jordan, P., 2017. “Real-time modelling of wavepackets in turbulent jets”. *Journal of Fluid Mechanics*, **821**, pp. 458–481.
- [122] Beneddine, S., Yegavian, R., Sipp, D., and Leclaire, B., 2017. “Unsteady flow dynamics reconstruction from mean flow and point sensors: an experimental study”. *Journal of Fluid Mechanics*, **824**, pp. 174–201.
- [123] Kopiev, V. F., Belyaev, I. V., Faranosov, G. A., Kopiev, V. A., Ostrikov, N., Zaytsev, M. Y., Akishev, Y. S., Grushin, M., Trushkin, N., Bityurin, V., et al., 2015. “Instability wave control in turbulent jet by acoustical and plasma actuators”. *Progress in Flight Physics—Volume 7*, **7**, pp. 211–228.
- [124] Sasaki, K., Tissot, G., Cavalieri, A. V., Silvestre, F. J., Jordan, P., and Biau, D., 2018. “Closed-loop control of a free shear flow: a framework using the parabolized stability equations”. *Theoretical and Computational Fluid Dynamics*, pp. 1–24.
- [125] Cavalieri, A. V. G., 2016. “Jet-noise control using wavepacket models”. In *Measurement, simulation and control of subsonic and supersonic jet noise*. von Karman Institute for Fluid Dynamics Lecture Series.
- [126] Semeraro, O., Lusseyran, F., Pastur, L., and Jordan, P., 2017. “Qualitative dynamics of wave packets in turbulent jets”. *Physical Review Fluids*, **2**(9), p. 094605.
- [127] Cavalieri, A. V., Jordan, P., Wolf, W. R., and Gervais, Y., 2014. “Scattering of wavepackets by a flat plate in the vicinity of a turbulent jet”. *Journal of sound and Vibration*, **333**(24), pp. 6516–6531.
- [128] Bychkov, O., and Faranosov, G., 2014. “On the possible mechanism of the jet noise intensification near a wing”. *Acoustical Physics*, **60**(6), pp. 633–646.
- [129] Faranosov, G. A., and Bychkov, O. P., 2017. “Two-dimensional model of the interaction of a plane acoustic wave with nozzle edge and wing trailing edge”. *The Journal of the Acoustical Society of America*, **141**(1), pp. 289–299.
- [130] Piantanida, S., Jaunet, V., Huber, J., Wolf, W. R., Jordan, P., and Cavalieri, A. V., 2016. “Scattering of turbulent-jet wavepackets by a swept trailing edge”. *The Journal of the Acoustical Society of America*, **140**(6), pp. 4350–4359.
- [131] Towne, A., Cavalieri, A. V., Jordan, P., Colonius, T., Schmidt, O., Jaunet, V., and Brès, G. A., 2017. “Acoustic resonance in the potential core of subsonic jets”. *Journal of Fluid Mechanics*, **825**, pp. 1113–1152.
- [132] Jordan, P., Jaunet, V., Towne, A., Cavalieri, A. V., Colonius, T., Schmidt, O., and Agarwal, A., 2018. “Jet-flap interaction tones”. *Journal of Fluid Mechanics*, **853**, pp. 333–358.
- [133] Lawrence, J., and Self, R. H., 2015. “Installed jet-flap impingement tonal noise”. In 21st AIAA/CEAS Aeroacoustics Conference, p. 3118.
- [134] Tam, C. K., and Ahuja, K., 1990. “Theoretical model of discrete tone generation by impinging jets”. *Journal of Fluid Mechanics*, **214**, pp. 67–87.
- [135] Bogey, C., and Gojon, R., 2017. “Feedback loop and upwind-propagating waves in ideally expanded supersonic impinging round jets”. *Journal of Fluid Mechanics*, **823**, pp. 562–591.
- [136] Shen, H., and W. Tam, C. K., 1998. “Numerical simulation of the generation of axisymmetric mode jet screech tones”. *AIAA journal*, **36**(10), pp. 1801–1807.
- [137] Edgington-Mitchell, D., Jaunet, V., Jordan, P., Towne, A., Soria, J., and Honnery, D., 2018. “Upstream-travelling acoustic jet modes as a closure mechanism for screech”. *Journal of Fluid Mechanics*, **855**.
- [138] Abreu, L. I., Cavalieri, A. V., and Wolf, W. R., 2017. “Coherent hydrodynamic waves and trailing-edge noise”. In 23rd AIAA/CEAS Aeroacoustics Conference, p. 3173.